

Coupled versus energetic nonlocal failure criteria: A case study on the crack onset from circular holes under biaxial loadings

*Original*

Coupled versus energetic nonlocal failure criteria: A case study on the crack onset from circular holes under biaxial loadings / Chao Correas, A.; Sapora, A.; Reinoso, J.; Corrado, M.; Cornetti, P.. - In: EUROPEAN JOURNAL OF MECHANICS. A, SOLIDS. - ISSN 0997-7538. - 101:(2023), pp. 1-20. [10.1016/j.euromechsol.2023.105037]

*Availability:*

This version is available at: 11583/2979778 since: 2023-07-03T08:20:29Z

*Publisher:*

Elsevier

*Published*

DOI:10.1016/j.euromechsol.2023.105037

*Terms of use:*

This article is made available under terms and conditions as specified in the corresponding bibliographic description in the repository

*Publisher copyright*

(Article begins on next page)



# Coupled versus energetic nonlocal failure criteria: A case study on the crack onset from circular holes under biaxial loadings

A. Chao Correas<sup>a,b,\*</sup>, A. Sapora<sup>a</sup>, J. Reinoso<sup>b</sup>, M. Corrado<sup>a</sup>, P. Cornetti<sup>a</sup>

<sup>a</sup> Department of Structural, Geotechnical and Building Engineering, Politecnico di Torino, Corso Duca degli Abruzzi 24, 10129, Turin, Italy

<sup>b</sup> Departamento de Mecánica de Medios Continuos y Teoría de Estructuras, ETS Ingeniería, Universidad de Sevilla, Camino de los Descubrimientos S/N, 41092, Sevilla, Spain

## ARTICLE INFO

### Keywords:

Finite fracture mechanics  
Cohesive zone model  
Phase field model of fracture  
Circular holes  
Biaxial loadings

## ABSTRACT

The phenomenon of brittle crack onset stemming from a circular hole in an infinite plate subjected to remote biaxial loading is herein investigated. A thorough analysis on the influence of the loading biaxiality reveals the existence of a wide casuistry in the sign and trend distributions of the stress field and Stress Intensity Factor, thus rendering it an exhaustive case study for assessing different failure criteria. Subsequently, three different approaches are used to determine the biaxial safety domains, two of which rely on the coupling of stress and energy conditions for failure, namely Finite Fracture Mechanics and Cohesive Zone Model, plus the purely energy-driven Phase Field model of fracture. Noteworthy, Finite Fracture Mechanics predicts the existence of a region in the loading space where failure is exclusively governed by the energy condition. Likewise, it is mathematically proven that the system of equations governing Dugdale's Cohesive Zone Model is equivalent to the first-order minimization condition of the energy balance, the resultant predictions being fairly close to those obtained by Finite Fracture Mechanics. Lastly, the Phase Field model of fracture is numerically implemented in the context of Finite Elements while paying special attention to the choice of the energy decomposition, whereof two are implemented: No-Decomposition and No-Tension decomposition. Specifically, the latter showcases satisfactory agreement with both Finite Fracture Mechanics and Dugdale's Cohesive Zone Model, thus posing a solid contender for studying complex fracture scenarios upon combined tension-compression stress states.

## 1. Introduction

Brittle failure arising from circular holes poses a big threat to the integrity of many critical structural components, such as the fuselage of aircraft or the pressure vessels used in nuclear reactors, to mention but a few. In many cases, these are quasi-bidimensional elements subjected to biaxial loading conditions in which the presence of circular holes leads to the concentration of the stresses therein. Consequently, the obtention of trustworthy failure predictions upon these conditions results essential for ensuring the structural integrity and operational readiness of critical pieces of machinery, thus posing a matter of great industrial interest.

In this regard, different works have addressed the onset of failure stemming from circular holes that are embodied in bidimensional domains. In particular, Leguillon and Piat (2008) utilized Finite Fracture Mechanics and the asymptotic matching technique to study the “key-hole” problem, in which a pre-existing crack is effectively toughened by the presence of a circular hole at its tip. Remarkably, the coupling of energy

and stress conditions for failure meant that the criterion could predict the size-effect in the effective toughening despite the geometry not being singular. Furthermore, Camanho et al. (2012) implemented the Finite Fracture Mechanics approach to study failure initiation in a uniaxially tensioned composite plate with finite dimensions and a central circular hole. Therein, the comparison with experimental results showed that indeed Finite Fracture Mechanics is able to better reproduce the experimental results in comparison with other failure criteria, such as the Theory of Critical Distances (Taylor, 2007). This same problem was also studied in Martin et al. (2012), where the Authors carried out parametric studies to determine the effect of the plate width, the material brittleness or the laminate's anisotropy, among others, on the failure predictions. In any case, they found good agreement between Finite Fracture Mechanics and the experimental results. A more complex setup was tackled by Rosendahl et al. (2017), where Finite Element implementations of the Finite Fracture Mechanics approach (and of the Cohesive Zone Model) were used to analyze the crack onset in a finite plate with a centered open hole under combined tension and bending loading conditions. Therein, it was shown

\* Corresponding author. Department of Structural, Geotechnical and Building Engineering, Politecnico di Torino, Corso Duca degli Abruzzi 24, 10129, Turin, Italy.  
E-mail address: [arturo.chaocorreas@polito.it](mailto:arturo.chaocorreas@polito.it) (A. Chao Correas).

Nomenclature			
$(r, \theta)$	Polar coordinates	$E$	Young's Modulus
$R$	Hole radius	$\nu$	Poisson's Ratio
$\Sigma_1, \Sigma_2$	Baseline remote stresses	$u_\theta, u_\theta^{\Sigma_1}$	Crack Mouth Opening Displacement
$\beta$	Baseline biaxiality ratio	$\Omega$	Structural domain
$\Sigma'_1, \Sigma'_2$	Surrogate remote stresses	$\vec{x}$	Generic position vector
$\beta'$	Surrogate biaxiality ratio	$\vec{u}$	Displacement vector field
$\sigma_{rr}, \sigma_{\theta\theta}, \tau_{r\theta}$	Stress components in polar coordinates	$\alpha$	Damage field
$S_{rr}, S_{\theta\theta}, S_{r\theta}$	Shape functions of the stress components in polar coordinates	$\Pi_{TOT}$	Total potential energy
$\sigma_I$	Crack opening stress component	$\Pi_S$	Strain component of the potential energy
$\sigma_C$	Tensile strength	$\Pi_F$	Fracture component of the potential energy
$\bar{\sigma}_{\theta\theta}$	Averaged crack opening stress component	$\Pi_{EXT}$	External work
$a$	Crack length	$\ell$	Phase Field's internal length
$a_p$	Process zone length	$a_{PF}$	Phase Field's Elastic degradation function
$K_I$	Mode I Stress Intensity Factor under biaxial loading	$w_{PF}$	Phase Field's Energy dissipation function
$\bar{K}_I$	Averaged Mode I Stress Intensity Factor under biaxial loading	$c_w$	Phase Field's dissipative scaling coefficient
$F_{\beta'}$	Shape function of the Mode I Stress Intensity Factor under biaxial loading	$\lambda, \mu$	Lamé constants
$K_I^{\sigma_C}$	Mode I Stress Intensity Factor under Constant Stress Lip loading	$\bar{\epsilon}$	Infinitesimal strain tensor
$F^{\sigma_C}$	Shape function of the Mode I Stress Intensity Factor under Constant Stress Lip loading	$\psi_0$	Undamaged strain energy density
$K_I^{\bar{P}}$	Mode I Stress Intensity Factor under Line-Load Edge loading	$\bar{\eta}$	Structured deformations tensor
$\bar{F}^{\bar{P}}, \bar{F}_A^{\bar{P}}$	Shape functions of the Mode I Stress Intensity Factor under Line-Load Edge loading	$L$	Characteristic dimension of the structural domain used for FE simulations
$K_{IC}$	Mode I fracture toughness	$\Gamma$	Geometrical locus of the cracked region
$G$	Strain Energy Release Rate	$h$	Characteristic element size
$G_C$	Fracture energy	$t_f$	"Instant" of failure
$l_{ch}$	Irwin's length	<b>Abbreviations</b>	
$\Delta_0$	Initial crack length/Initial configuration	FFM	Original version of the Finite Fracture Mechanics approach
$\Delta$	Incremental crack length	FFM-avg	Averaged stress version of the Finite Fracture Mechanics approach
$\Sigma_{1f}, \Sigma_{2f}$	Baseline failure remote stresses	CZM	Dugdale's version of the Cohesive Zone Model
$\Sigma'_{1f}, \Sigma'_{2f}$	Surrogate failure remote stresses	PF-NoSplit	Phase Field model of fracture without energy decomposition
$\Delta_f$	Critical length	NS	No Split (referred to the PF-NoSplit)
$\hat{\sigma}_{\theta\theta, f}$	Normalized maximum crack opening stress at instant of failure onset	PF-NoTension	Phase Field Model of fracture with the No Tension energy decomposition
		NT	No Tension (referred to the PF-NoTension)
		SIF	Stress Intensity Factor
		FE	Finite Element
		CMOD	Crack Mouth Opening Displacement
		CSL	Constant Stress Lip loading
		LLE	Line-Load Edge loading

that the either symmetric or asymmetric nature of the crack initiation depends upon the loading case considered. Moreover, reasonable agreement in the crack onset predictions by Finite Fracture Mechanics and Cohesive Zone Model was therein reported. In this same line, [Sapora et al. \(2018\)](#) exploited a fully analytical implementation of Finite Fracture Mechanics and of Theory of Critical Distances to assess whether symmetric or asymmetric crack propagation is preferential for a fracture stemming from a circular hole under remote uniaxial tension. Indeed, they showed that while stress-based criteria cannot distinguish among the two cracking configurations, Finite Fracture Mechanics states that the symmetric crack onset is preferable for that it yields a slightly lower failure load. Once again, Finite Fracture Mechanics' good agreement with experiments conducted in isotropic, homogeneous and brittle materials was reported. Other relevant works using the Finite Fracture Mechanics approach include the recent studies by [Doitrand and Leguillon \(2021\)](#) on the crack onset from a circular hole close to a free edge, and by [Weißgraeber et al. \(2016\)](#) on the crack onset from elliptical holes, both of them under uniaxial loading conditions.

The good performance showcased by Finite Fracture Mechanics in the uniaxial loading case, among others, paved the way to its application

to the much more complex biaxial counterpart, and a first attempt to assess the interaction between remote biaxial loading and a circular hole was done in [Torabi et al. \(2017\)](#). In this work, the biaxial loading conditions were generated via Brazilian disk specimens with a central circular hole: the "remote" stress along the loading axis was in compression and its magnitude was three times larger than the "remote" tensile one along the perpendicular axis. As a result, the analysis was limited to one single biaxiality ratio, which once more showcased the good agreement of Finite Fracture Mechanics predictions with experiments. This analysis was taken further in [Sapora and Cornetti \(2018\)](#), in which the biaxiality ratio was no longer fixed, but considered as a problem parameter. Interestingly, it was reported that the biaxiality ratio could completely change the nature of the problem by modifying the trend and sign of the stress field and the Stress Intensity Factor. Aiming to assess the accuracy of Finite Fracture Mechanics against biaxial experimental results available in the literature, the Authors focused on the tension-tension and tension-compression remote loading configurations. Likewise, no continuous analysis of the effect of the biaxiality ratio was made, focusing instead on the failure size-effect for certain biaxiality ratios of interest.

Besides Finite Fracture Mechanics, the application of other well-established failure criteria to the problem under study remains scarce. For instance and to the authors' best knowledge, so far just Li and Zhang (2006) and Ferrian et al. (2022) have analytically implemented the Cohesive Zone Model to assess the size-effect on the effective strength, although both studies were limited to the uniaxial tension case. In this sense, the work by Chao Correias et al. (2021) results insightful for that the Authors introduced a novel procedure that allows to implement Dugdale's Cohesive Zone Model (Dugdale, 1960) in a semianalytical way for a wide range of geometries and loadings.

On the other hand, the implementation of more sophisticated computational fracture criteria is also of interest herein, namely the invogue approach of the Phase Field model of fracture. Firstly conceptualized in Francfort and Marigo (1998) and then numerically implemented by Bourdin et al. (2000), the Phase Field modelling of fracture has garnered large shares of interest in the computational fracture mechanics community ever since, given its strong theoretical foundation and virtual devoidness of the drawbacks of other main failure/fracture criteria, such as the mesh dependency or the necessity to know the crack path *a priori*. Remarkably, this purely energy-based approach presents a dual nature: on one hand, it acts as a Gradient Damage Model in what concerns to crack initiation; on the other, it represents the regularization of the Griffith problem once into the crack propagation regime. Clearly, it is the former nature of the methodology that results the most interesting herein. In this regard, different studies have compared the Phase Field models of fracture with Finite Fracture Mechanics towards assessing the former's performance with regards to crack onset predictions. For instance, one can mention the relevant works by Reinoso et al. (2017) on thin ply laminates containing a circular hole under uniaxial tension, by Strobl and Seelig (2020) on Hertzian indentation fracture, and by Abaza et al. (2022) on porous materials. Furthermore, the establishment of a dialogue between Finite Fracture Mechanics and Phase Field models of fracture was put forward in Doitrand et al. (2023) by considering the latter's regularization length as a function determined by the strength predictions of the former. Concerning more specifically to the Phase Field modelling of fracture, there must be herein highlighted the thorough work by De Lorenzis and Maurini (2022), where the concept of strain energy decomposition is widely covered and the crack nucleation predictions of different specific formulations were presented under multiaxial loading conditions. In fact, their focus was set on comparing their intrinsic differences, i.e. not related to the geometry under study, and the conclusions were clear: the importance of choosing proper energy decompositions increases upon more complex loading cases. Likewise, cracking predictions by the Phase Field modelling of fracture have been experimentally corroborated by Cavuoto et al. (2022), in which the failure patterns resulting from defect interaction (including notches and circular holes) were studied in different complex mechanical configurations, wherein traction and traction-compression stress states took place.

In light of the previous discussion, the present work will be devoted to the application of state-of-the-art failure criteria to the problem of crack nucleation stemming from a circular hole embedded in an infinite and bidimensional plane strain domain under biaxial loading conditions. In particular, the present analysis will concern the following approaches: Finite Fracture Mechanics, Cohesive Zone Model and Phase Field model of fracture. The intended outcome from this research is twofold: (i) to provide the hole size-dependent biaxial safety domains predicted by different well-established criteria; (ii) to exploit the wide range of stress and energy conditions occurring in the geometry at hand to get a sound and exhaustive comparison between different failure criteria. To this goal, the following work is articulated in five Sections. Section 2 contains a thorough description of the characteristics of the problem under investigation as to fully comprehend its features and complexities. Sections 3, 4 and 5 are devoted to the description and implementation of the frameworks of Finite Fracture Mechanics, Cohesive Zone Model and Phase Field model of fracture, respectively, with

special attention being paid to comparing their differences with regards to the predicted safety domains. Lastly, final conclusions are drawn in Section 6.

## 2. The biaxial loading problem in a slab containing a circular hole

Devoting the present analysis to isotropic and homogeneous materials that showcase linear elastic behavior up to brittle failure, the biaxial loading conditions can be treated as resulting from the superposition of two perpendicular uniaxial loading cases. This, particularized for the case of an infinite slab containing a circular hole, is schematically depicted in Fig. 1 (a). Therein,  $\Sigma_1$  and  $\Sigma_2$  stand for the imposed remote stresses in each of the loading directions, respectively. In turn, these represent the most straightforward pair of values that univocally identifies each biaxial loading state. Subsequently, the set of all their possible combinations defines a bidimensional  $(\Sigma_1 - \Sigma_2)$  loading space. Likewise, it is noteworthy that the studied problem is symmetric with respect to the  $\Sigma_1 = \Sigma_2$  loading states, thus allowing to just explicitly consider a subregion of the whole loading space, e.g. where  $\Sigma_1 \geq \Sigma_2$ , without affecting the completeness of the study.

Nonetheless, the definition of the problem in terms of  $\Sigma_1$  and  $\Sigma_2$  results inadequate for depicting the crack onset dependence with the biaxial loading states. Instead, it is more convenient to introduce two different parameters: one governing the magnitude of the loading and another one ruling its degree of biaxiality. In this sense, the formulation used by Tada et al. (2000) and Sapora and Cornetti (2018) kept  $\Sigma_1$  as a measure of the loading level, while the biaxiality was controlled by the ratio  $\beta = \Sigma_2/\Sigma_1$ . However, for the subregion of interest of the  $(\Sigma_1 - \Sigma_2)$  loading space, viz.  $\Sigma_1 \geq \Sigma_2$ ,  $\beta$  does not have a convenient definition since it presents an infinite discontinuity at the locus of uniaxial compressive states  $\Sigma_1 = 0 > \Sigma_2$ . Note that Sapora and Cornetti (2018) only explored the quadrants of the loading space where at least one remote stress is positive, so that the above mentioned inconvenience in using  $\beta$  did not come into play therein.

To avoid this limitation, a  $(\Sigma'_1 - \Sigma'_2)$  surrogate loading space is herein introduced by rotating  $\pi/4$  radians clockwise the  $(\Sigma_1 - \Sigma_2)$  baseline loading space, as shown in Fig. 1 (b). Mathematically, the mapping between the baseline and surrogate loading spaces is nothing but the vector rotation transformation given in Eq. (1).

$$\begin{pmatrix} \Sigma'_1 \\ \Sigma'_2 \end{pmatrix} = \frac{1}{\sqrt{2}} \begin{bmatrix} 1 & -1 \\ 1 & 1 \end{bmatrix} \begin{pmatrix} \Sigma_1 \\ \Sigma_2 \end{pmatrix} \quad (1)$$

In such manner, the use of the  $(\Sigma'_1 - \Sigma'_2)$  surrogate loading space allows to access every possible biaxiality state of interest, by tuning a single and continuously defined parameter  $\beta' = \Sigma'_2/\Sigma'_1$  |  $\beta' \in (-\infty, \infty)$ , whereas the intensity of the load is determined by the parameter  $\Sigma'_1$ . In addition, for  $\beta'$  being defined analogously to  $\beta$ , the former will be hereinafter called surrogate biaxiality ratio. Clearly, the mathematical relation between both parameters is governed by the transformation in Eq. (1) and particularizes in the expressions shown in Eq. (2).

$$\beta' = \frac{1+\beta}{1-\beta} \quad ; \quad \beta = \frac{-1+\beta'}{1+\beta'} \quad (2)$$

On the other hand,  $\Sigma'_1$  being strictly positive for  $\Sigma_1 > \Sigma_2$ , any to-be-performed analysis on the sign distribution of the magnitudes of interest considerably simplifies since only its dependence with  $\beta'$  needs consideration. From a physical perspective, it is highlighted that biaxiality is achieved in the surrogate loading space by the superposing pure shear and plane hydrostatic states, governed by  $\Sigma'_1$  and  $\Sigma'_2$ , respectively. Moreover, the most distinctive loading cases correspond to the following characteristic values of the surrogate biaxiality ratio:  $\beta' = \pm\infty$  stand for either uniform bi-tension or bi-compression states,  $\beta' = \pm 1$  correspond

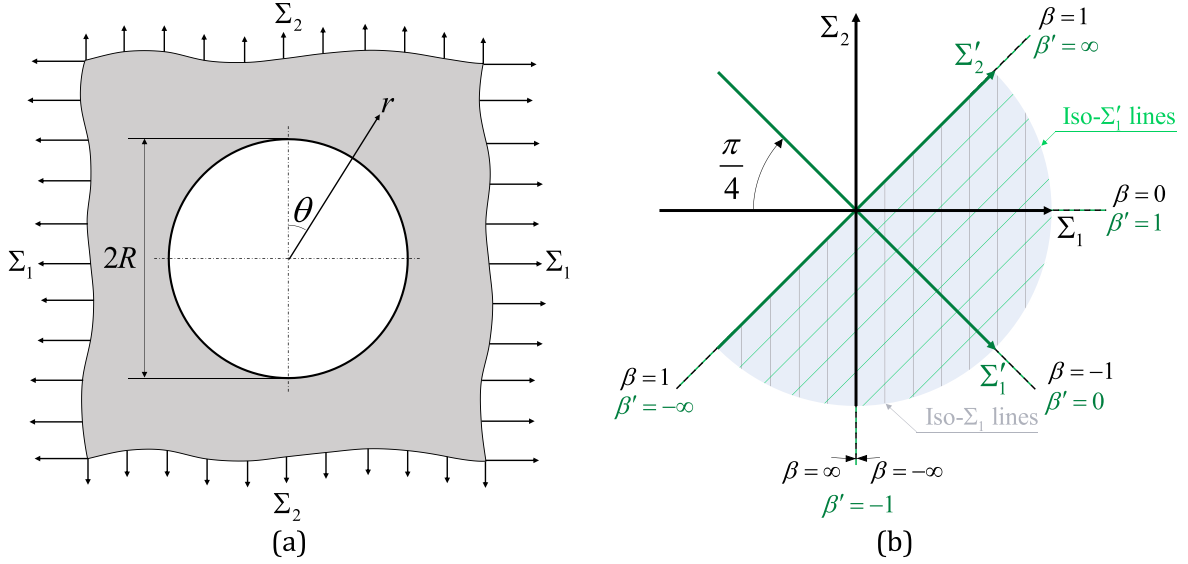


Fig. 1. (a) Schematic representation of an infinite slab containing a circular hole under biaxial loading; (b) Representation of the baseline (black) and surrogate (green) loading spaces.

to either uniaxial tension or compression, and lastly,  $\beta' = 0$  represents pure shear loading states. Eventually, it should be noted that the procedure above presented is not the only one that allows defining all the biaxial loading cases of interest with a single and continuously defined parameter. In this sense, there can be highlighted the work by Mantić et al. (2015), in which they introduced a biaxiality parameter that represented the position of the center of the normalized Mohr's circle in the remote regions of the domain.

### 2.1. Stress field

Based on the work by Kirsch (1898) and using the superposition principle, the definition in polar coordinates of the stress field components in the surroundings of a circular hole embedded in an infinite bidimensional domain that is subjected to biaxial loading conditions results as in Eqs. (3)–(5), where the surrogate load  $\Sigma_1'$  and biaxiality ratio  $\beta'$  are the loading parameters.

$$\sigma_{rr}(r, \theta, \Sigma_1', \beta') = \frac{\Sigma_1'}{\sqrt{2}} \left\{ \beta' \left[ 1 - \left( \frac{R}{r} \right)^2 \right] + \left[ 1 - 4 \left( \frac{R}{r} \right)^2 + 3 \left( \frac{R}{r} \right)^4 \right] \cos 2\theta \right\} = \Sigma_1' S_{rr}(r, \theta, \beta') \quad (3)$$

$$\sigma_{\theta\theta}(r, \theta, \Sigma_1', \beta') = \frac{\Sigma_1'}{\sqrt{2}} \left\{ \beta' \left[ 1 + \left( \frac{R}{r} \right)^2 \right] + \left[ 1 + 3 \left( \frac{R}{r} \right)^4 \right] \cos 2\theta \right\} = \Sigma_1' S_{\theta\theta}(r, \theta, \beta') \quad (4)$$

$$\tau_{r\theta}(r, \theta, \Sigma_1') = \frac{\Sigma_1'}{\sqrt{2}} \left[ 1 + 2 \left( \frac{R}{r} \right)^2 - 3 \left( \frac{R}{r} \right)^4 \right] \sin 2\theta = \Sigma_1' S_{r\theta}(r, \theta) \quad (5)$$

Thereby, it becomes clear that while the normal components of the stress field, i.e.  $\sigma_{rr}$  and  $\sigma_{\theta\theta}$ , depend on both  $\Sigma_1'$  and  $\beta'$ , the shear stress  $\tau_{r\theta}$  only depends on  $\Sigma_1'$  (i.e. with the pure shear component of the loading). At the same time, it turns out that both  $\sigma_{rr}$  and  $\sigma_{\theta\theta}$  are maximized with respect to  $\theta$  when  $\theta = 0$  and  $\theta = \pi$  for the loading cases of interest. This implies that, for the considered geometry and loading setup, crack onset is expected to always develop at the  $\theta = 0$  and  $\theta = \pi$  radial directions for failures governed by direct stresses (such as that of brittle materials). In turn, the shear stress component vanishes along these azimuths, thus leaving the expected crack onset to develop upon pure Mode I

conditions. Further analysis on the dependence that the function  $\sigma_{\theta\theta}(r, \theta = \{0, \pi\}) = \sigma_{\theta\theta}(r)$  presents with the surrogate biaxiality ratio  $\beta'$  will be carried out in Section 2.3.

### 2.2. Stress intensity factor

The analytical approximate expressions of the Mode I Stress Intensity Factor (SIF) for the cases of a single radial crack (asymmetric cracking) or two antipodal twin cracks (symmetric cracking) stemming from a circular hole in a biaxially-loaded slab were given by Tada et al. (2000). In this regard, there can be proven that the symmetric failure configuration is energetically preferred as for leading to a higher total release upon crack propagation, this outcome being aligned with the conclusions of the work by Sapora et al. (2018) on the circular hole problem under uniaxial tension. Likewise, given that  $\theta = 0$  and  $\theta = \pi$  are the highest stressed regions within the domain, the cracks upon failure will be limited to grow in those directions. Using the mapping in Eq. (1), the approximate SIF expression in terms of  $\Sigma_1'$  and  $\beta'$  for a pair of symmetric antipodal cracks, each one of length  $a$  and stemming in the directions  $\theta = 0$  and  $\theta = \pi$  from the circular hole results as in Eqs. (6)–(9), where  $\xi = a/(a + R)$ .

$$K_I(a, \Sigma_1', \beta') = \Sigma_1' \sqrt{\pi a} F_{\beta'}(a, \beta') \quad (6)$$

$$F_{\beta'}(a, \beta') = \sqrt{2} \left[ F_0(\xi) + \frac{\beta' - 1}{2} F_1(\xi) \right] \quad (7)$$

$$F_0(\xi) = 0.5(3 - \xi) [1 + 1.243(1 - \xi)^3] \quad (8)$$

$$F_1(\xi) = 1 + (1 - \xi) [0.5 + 0.743(1 - \xi)^2] \quad (9)$$

Noteworthy, the approximate functions  $F_0$  and  $F_1$  were reported to yield an error of 1%. Therefore, the SIF shape function  $F_{\beta'}$  depends on the surrogate biaxiality ratio  $\beta'$  and on two functions  $F_0$  and  $F_1$  which are just dependent on the crack length  $a$  and the hole radius  $R$ . For any value of  $a$  and fixed  $R$ ,  $F_0$  is greater than  $F_1$ , and their difference monotonically decreases from  $F_0 \approx 1.5F_1$  as  $a \rightarrow 0$  down to  $F_0 = F_1$  as  $a \rightarrow \infty$ . As a result,  $F_{\beta'}$  ceases to be positive only for sufficiently large negative values of  $\beta'$ , as shown in the following section.



### 2.3. $\beta'$ -dependence

From previous sections it is clear that, by modifying the degree of biaxiality  $\beta'$ , the sign and trend of the stress components and the SIF change, and with them, the crack onset conditions. This results in the need of properly addressing all the different crack onset regimes that may appear. In this sense, the present section highlights the dependence in sign and trend that the relevant stress and SIF quantities have on  $\beta'$ .

Hereafter, four quantities will be analyzed:  $\sigma_{\theta\theta}$ ,  $K_I$ ,  $\tilde{\sigma}_{\theta\theta}$  and  $\tilde{K}_I$ . The latter two will be relevant for the subsequent application of the Finite Fracture Mechanics approach, and their definitions are given in Eqs. (10) and (11), respectively.

$$\tilde{\sigma}_{\theta\theta}(r) = \Sigma'_1 \left[ \frac{1}{r-R} \int_R^r S_{\theta\theta}(r') \, dr' \right] \quad \text{for } r \geq R \quad (10)$$

$$\tilde{K}_I(a) = \Sigma'_1 \sqrt{\pi} \sqrt{\frac{1}{a} \int_0^a a' [F_{\beta'}(a', \beta')]^2 \, da'} \quad (11)$$

Plainly, the former represents the arithmetic average of the hoop stress  $\sigma_{\theta\theta}$  over the range  $R \leq r' \leq r$ , whereas the latter is the quadratic average of the SIF  $K_I$  over the range  $0 \leq a' \leq a$ . The ranges of  $\beta'$  that lead to different evolutions of the sign or the trend of the quantities of interest are then detailed in Table 1. Therein, the signs + or – stand for positive or negative values, respectively, while the  $\nearrow$  or  $\searrow$  arrows indicate either monotonically increasing or decreasing trends. Likewise, the sequence of symbols from left to right represent the evolution of the analyzed magnitude's feature as either  $r$  or  $a$  grows. For instance, when  $\beta' \in (-1, 6 - 4\sqrt{3})$ ,  $\sigma_{\theta\theta}(r)$  presents the sign distribution + – +, meaning that  $\sigma_{\theta\theta}(r)$  is positive in the surroundings of the hole ( $r \approx R$ ), but as  $r$  grows it first turns negative and then goes back to positive. In the same  $\beta'$  range, the trend for  $\sigma_{\theta\theta}(r)$  is  $\searrow \nearrow$ , implying that  $\sigma_{\theta\theta}$  monotonically decreases as  $r$  grows from  $R$  up to a critical value, from which onwards it increases monotonically with  $r$ .

For the sake of absolute conciseness, the graphical description of the  $\sigma_{\theta\theta}$ ,  $K_I$ ,  $\tilde{\sigma}_{\theta\theta}$  and  $\tilde{K}_I$  curves within the different ranges of  $\beta'$  reported in Table 1 is provided in Fig. 2.

It results clear that by considering a biaxial loading scenario, the casuistry in terms of the evolution of the stress field and the energy release is largely enriched with respect to that corresponding to the simple uniaxial loading case ( $\beta' = 1$ ), for instance. Indeed, the presence of local extrema in both  $\sigma_{\theta\theta}$  and  $K_I$  (as well as in their averages  $\tilde{\sigma}_{\theta\theta}$  and  $\tilde{K}_I$ ), added to the variety in their trend evolution, is expected to trigger some features of the considered failure criteria that would remain hid-

den for simpler setups. This renders the considered case study convenient to test and compare the different failure criteria under a wide range of completely different prospective failure conditions upon just the change of the scalar parameter  $\beta'$ .

### 3. Finite Fracture Mechanics

The well-known Finite Fracture Mechanics criterion (Cornetti et al., 2006; Leguillon, 2002) hypothesizes that failure initiation is a phenomenon that develops instantaneously in time and by finite increments in space. Crack onset is assumed to be triggered at the minimum load at which both stress and energy nonlocal conditions are simultaneously fulfilled over any potential finite fracture surface. As a result, Finite Fracture Mechanics criterion mathematically reads as a minimization problem subjected to nonlocal conditions in which both size and shape of the critical finite region, often identified as the fracture initiation surface, are not inputs but outputs. This allows the criterion to interplay with the structure, rendering it more robust and potentially applicable to any setup, although at the cost of increased complexity. Nonetheless, when the Finite Fracture Mechanics approach is applied to bidimensional scenarios in which the prospective crack path is known (as the one here at hand), the problem can be entirely defined in terms of two scalar unknowns: the in-plane crack length and the magnitude of the loading. Consequently, its resolution is considerably simplified with respect to the generic case.

While the discrete energy balance is unique, there exists two main Finite Fracture Mechanics variants depending on the non local stress condition to be used: one is the original proposal by Leguillon (2002), and the other is the average-stress variant introduced in Cornetti et al. (2006). In what follows, both formulations will be particularized for the problem under investigation. For the sake of clarity, please note that whenever the complete name of the approach is used onwards, e.g. Finite Fracture Mechanics, the respective statement applies to the framework as a whole. In contrast, whenever only one of the variants within the framework is referred to, the corresponding acronym will be used, e.g. FFM and FFM-avg.

#### 3.1. Original formulation (FFM)

In the Finite Fracture Mechanics' formulation proposed by Leguillon (2002) (FFM), the stress condition for failure requires the pre-failure crack opening stress component  $\sigma_I$  to be greater than the material strength  $\sigma_C$  all along the region of prospective crack growth. At the same time, it is required that the amount of energy released during fracturing is larger than the material fracture energy  $G_C$  multiplied by the newly

**Table 1**

Dependence with  $\beta'$  of the evolution of the sign and trend of  $\sigma_{\theta\theta}$ ,  $\tilde{\sigma}_{\theta\theta}$ ,  $K_I$  and  $\tilde{K}_I$ .

$\sigma_{\theta\theta}(r)$				$\tilde{\sigma}_{\theta\theta}(r)$			
$\beta'$ ranges	Sign	Trend	Tag	$\beta'$ ranges	Sign	Trend	Tag
$\beta' \in (-\infty, -6)$	–	$\nearrow$	A1	$\beta' \in (-\infty, -6)$	–	$\nearrow$	B1
$\beta' \in (-6, -2)$	–	$\searrow \nearrow$	A2	$\beta' \in (-6, -2)$	–	$\searrow \nearrow$	B2
$\beta' \in (-2, -1)$	+ –	$\searrow \nearrow$	A3	$\beta' \in (-2, -1)$	+ –	$\searrow \nearrow$	B3
$\beta' \in (-1, 6 - 4\sqrt{3})$	+ – +	$\searrow \nearrow$	A4	$\beta' \in (-1, \infty)$	+	$\searrow$	B4
$\beta' \in (6 - 4\sqrt{3}, 0)$	+	$\searrow \nearrow$	A5				
$\beta' \in (0, \infty)$	+	$\searrow$	A6				
$K_I(a)$				$\tilde{K}_I(a)$			
$\beta'$ ranges	Sign	Trend	Tag	$\beta'$ ranges	Sign	Trend	Tag
$\beta' \in (-\infty, -2)$	–	$\searrow$	C1	$\beta' \in (-\infty, -2)$	+	$\nearrow$	D1
$\beta' \in (-2, -1)$	+ –	$\nearrow \searrow$	C2	$\beta' \in (-2, -1)$	+	$\nearrow \searrow$	D2
$\beta' \in (-1, -0.194)$	+	$\nearrow \searrow \nearrow$	C3	$\beta' = -1$	+	$\nearrow \searrow$	D3
$\beta' \in (-0.194, \infty)$	+	$\nearrow$	C4	$\beta' \in (-1, -0.443)$	+	$\nearrow \searrow \nearrow$	D4
				$\beta' \in (-0.443, \infty)$	+	$\nearrow$	D5

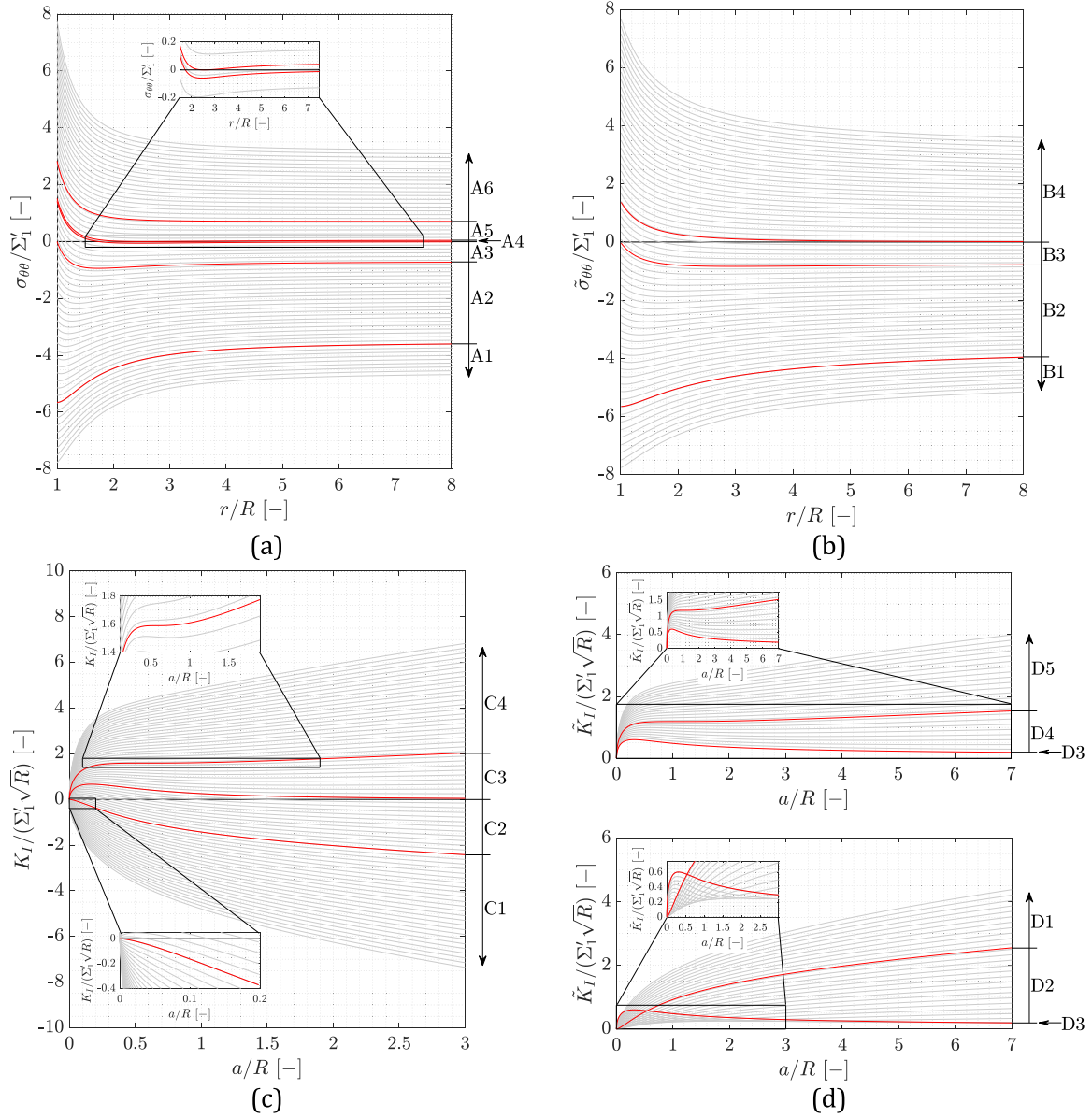


Fig. 2. Graphic representation of the dependence with  $\beta'$  of the evolution of the sign and trend of  $\sigma_{\theta\theta}$ ,  $\bar{\sigma}_{\theta\theta}$ ,  $K_I$  and  $\tilde{K}_I$  reported in Table 1.

created finite fracture surface. Therefore, the FFM's conditioned minimization problem can be mathematically defined for a generic bidimensional and biaxial problem as in Eq. (12), where:  $G$  is the Strain Energy Release Rate;  $\Delta_0$  and  $\Delta_0 + \Delta$  represent the geometrical states of the structural domain prior and after the crack grows by an arc length  $\Delta$ , respectively; and  $C_{\Delta_0+\Delta}^{\Delta_0}$  stands for the section of the crack path along which the crack propagation of length  $\Delta$  takes place.

$$\Sigma'_{lf} = \operatorname{argmin}(\Sigma'_1 \in S'); \quad \Sigma'_{2f} = \beta' \Sigma'_{1f}; \quad \Delta_f = \Delta(\Sigma'_{1f}, \beta')$$

$$\text{where } S' := \left\{ \Sigma'_1 \left| \Sigma'_1 : \left[ \sigma_I(r, \theta, \Sigma'_1) \geq \sigma_c \forall (r, \theta) \in C_{\Delta_0+\Delta}^{\Delta_0} \right] \right. \right\} \quad (12)$$

Given that the problem herein analyzed showcases failure in pure Mode I (See Section 2.1), the energy condition can be expressed in terms of the SIF  $K_I$  and the fracture toughness  $K_{IC}$  by virtue of the Irwin's Relation ( $\{G, G_c\} = \{K_I, K_{IC}\}^2 / E'$ , where  $E' = E / (1 - \nu^2)$  for plane strain, being  $E$  the Young's Modulus and  $\nu$  the Poisson's ratio), thus allowing to define the FFM discrete energy balance in terms of the  $K_I$  given in Eq.

(6). Likewise, the crack opening stress component  $\sigma_I$  herein corresponds to the hoop stress  $\sigma_{\theta\theta}$  defined in Eq. (3). As a result, the generic FFM formulation in Eq. (12) particularizes to Eq. (13) for the case at hand, where  $l_{ch} = K_{IC}^2 / \sigma_c^2$  and the crack path section  $C_{\Delta_0+\Delta}^{\Delta_0}$  is a pair of straight lines along  $\theta = 0$  and  $\theta = \pi$  so that  $R \leq r \leq R + \Delta$ . Noteworthy, Eq. (13) define the failure onset state in the surrogate loading space, and thus the inverse of the mapping in Eq. (1) should be used to obtain the failure states in the baseline loading space.

$$\frac{\Sigma'_{lf}}{\sigma_c} = \operatorname{argmin} \left( \frac{\Sigma'_1}{\sigma_c} \in \hat{S} \right); \quad \frac{\Sigma'_{2f}}{\sigma_c} = \beta' \frac{\Sigma'_{1f}}{\sigma_c}; \quad \Delta_f = \Delta \left( \frac{\Sigma'_{1f}}{\sigma_c}, \beta' \right)$$

$$\text{where } \hat{S} := \left\{ \frac{\Sigma'_1}{\sigma_c} \left| \frac{\Sigma'_1}{\sigma_c} : \left[ \begin{array}{l} \frac{\Sigma'_1}{\sigma_c} \geq \frac{1}{\min(S_{\theta\theta}(r, \beta')|_{\theta=0}, \forall r \in [R, R+\Delta])} \\ \frac{\Sigma'_1}{\sigma_c} \geq \sqrt{\frac{l_{ch} \Delta}{\pi \int_0^\Delta a [F_{\beta'}(a, \beta')]^2 da}} \end{array} \right] \right. \right\} \quad (13)$$

Differently from simpler setups in which the stress field is

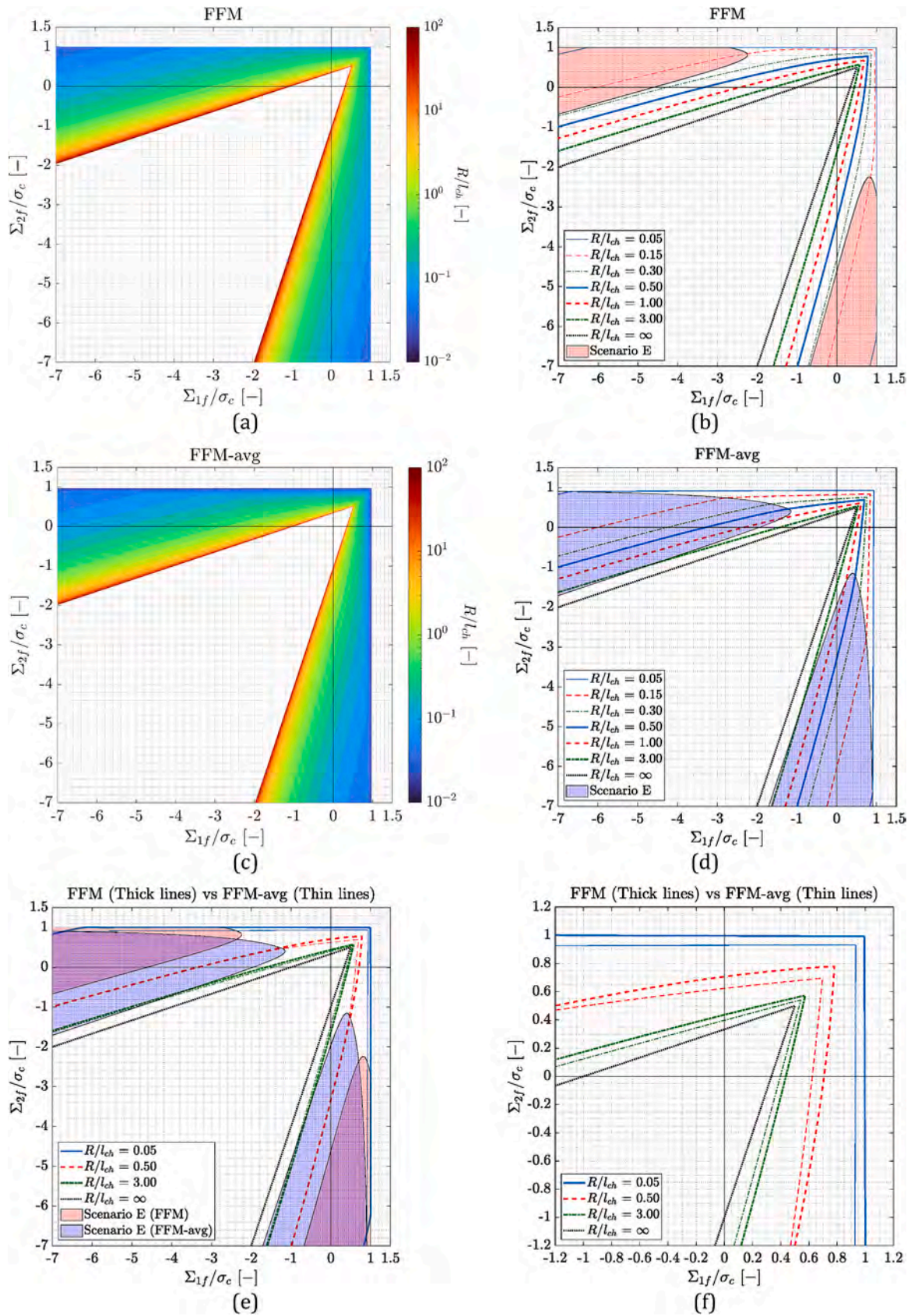


**Fig. 3.** Safety domains and failure scenarios as predicted by FFM (a, b) and FFM-avg (c, d). Comparison between FFM and FFM-avg predictions (e, f). Subfigures (b, d, f) are closeups of subfigures (a, c, e), respectively.



monotonically increasing and the geometry is positive ( $\partial G/\partial a > 0$ ), the wide casuistry in the evolution of  $\sigma_{\theta\theta}(r)$  and  $K_I(a)$  –as reported in Table 1– often impedes the usual simplification of the FFM's conditioned minimization problem to a system of two equations with two unknowns, i.e. where the inequalities in Eq. (13) become equalities. In particular, this simplification, which means that the solution corresponds to the intersection of the stress and energy conditions, results only possible for  $\beta' > 0.443$  according to Section 2.3. For lower values of  $\beta'$ , the local minimum of the energy condition's right hand side term in Eq. (13) is also a potential solution, and so, it must be calculated and compared against the aforementioned intersection: the lowest failure load corresponds to the solution of Eq. (13). Clearly, this procedure is easily solvable in a semianalytical manner. Additionally, it should be noted that the minimum operator in the denominator of the stress condition in Eq. (13) implies that the load magnitude strictly fulfilling the stress criterion will be monotonically increasing with  $\Delta$ . This, added to  $\sigma_{\theta\theta}(r)$  presenting a single local extremum in form of a local minimum when  $\beta' < 0$ , means that FFM can predict the crack onset stemming from the hole as occurring at  $\Sigma_{1f} > \sigma_c$  for small enough hole sizes. In those cases, the trivial no-hole solution should be explicitly incorporated in the FFM's failure load minimization procedure, thus reverting to the expected  $\Sigma_{1f} = \sigma_c$ . At the same time, the stress condition restricts failure to develop where the crack opening stress component is strictly tensile.

### 3.2. Average stress formulation (FFM-avg)

The other major formulation of Finite Fracture Mechanics, the so-called average stress variant (FFM-avg), was proposed by Cornetti et al. (2006) as a result of coupling the Neuber-Novozhilov stress criterion with the finite energy balance. In this sense, FFM-avg states that the magnitude to be larger than  $\sigma_c$  upon failure onset is the average of  $\sigma_I$  over the prospective crack growth surface. Consequently, the mathematical formulation of the FFM-avg for the generic bidimensional and biaxial loading problem is given in Eq. (14), resulting clear that both FFM and FFM-avg approaches only differ in the stress condition. Remarkably, the averaging of the stress component over  $C_{\Delta_0}^{\Delta_0+\Delta}$  improves the smoothness of the stress criterion in comparison with that of FFM, which despite being defined non-locally still relies on point-wise stress values. This smoothing effect can be properly understood by comparing the sign and trend evolutions of  $\sigma_{\theta\theta}$  and  $\bar{\sigma}_{\theta\theta}$  given in Table 1, and it materializes in simplified numerical resolution of the semi-analytical FFM-avg formulation in comparison with that of FFM. More importantly, averaging  $\sigma_I$  along  $\Delta$  implies that the “trivial” solution corresponding to the absence of a stress raiser is inherently considered in the minimization procedure.

$$\Sigma'_{1f} = \operatorname{argmin}(\Sigma'_1 \in \hat{S}'); \quad \Sigma'_{2f} = \beta' \Sigma'_{1f}; \quad \Delta_f = \Delta(\Sigma'_{1f}, \beta')$$

$$\text{where } \hat{S}' := \left\{ \Sigma'_1 \left| \Sigma'_1 : \begin{cases} \int_{C_{\Delta_0}^{\Delta_0+\Delta}} \sigma_I(r, \Sigma'_1) ds \geq \sigma_c \Delta \\ \int_{\Delta_0}^{\Delta_0+\Delta} G(a, \Sigma'_1) da \geq G_c \Delta \end{cases} \right. \right\} \quad (14)$$

Lastly, the particularization of the FFM-avg formulation for the considered problem is given in Eq. (15). Just as before, the obtained results need to be transformed from the surrogate to the baseline loading space. At the same time, the simplification to a system of two equations remains only possible when  $\beta' > 0.443$ , Eq. (15) being solvable analogously to Eq. (13).

$$\Sigma'_{1f} = \operatorname{argmin}(\Sigma'_1 \in \hat{S}'); \quad \Sigma'_{2f} = \beta' \Sigma'_{1f}; \quad \Delta_f = \Delta(\Sigma'_{1f}, \beta')$$

$$\text{where } \hat{S}' := \left\{ \Sigma'_1 \left| \Sigma'_1 : \begin{cases} \frac{\Sigma'_1}{\sigma_c} \geq \frac{\Delta}{\int_R^{R+\Delta} S_{\theta\theta}(r, \beta')|_{\theta=0} dr} \\ \frac{\Sigma'_1}{\sigma_c} \geq \frac{l_{ch} \Delta}{\sqrt{\pi \int_0^\Delta a [F_{\beta'}(a, \beta')]^2 da}} \end{cases} \right. \right\} \quad (15)$$

### 3.3. Implementation

The resultant safety domains as predicted by both FFM and FFM-avg approaches are depicted in Fig. 3 with the ratio  $R/l_{ch}$  as a parameter. Herein, the term “safety domain” stands for the geometrical locus of the loading space that contains the failure initiation states ( $\Sigma_{1f}$ ,  $\Sigma_{2f}$ ) for each hole size, i.e. for fixed  $R/l_{ch}$ . At the same time, the iso-biaxiality states are represented in the loading space by spokes stemming out from the origin, so that the further from it, the more intense the loading. Therefore, the failure initiation state ( $\Sigma_{1f}$ ,  $\Sigma_{2f}$ ) for a given hole size and load biaxiality is found at the intersection of the respective safety domain and iso-biaxiality spoke. As a consequence, any loading state ( $\Sigma_1$ ,  $\Sigma_2$ ) lying in a certain iso-biaxiality spoke, but closer to the origin than the respective failure state, rests within the safety domain and is thus deemed safe.

Interestingly, both criteria yield safety domains that are qualitatively tantamount, although FFM-avg is more conservative than FFM, a feature in line with what obtained for other configurations in the literature, e.g. (Chao Correias et al., 2021). Indeed, as previously indicated in Section 3.1, in some cases FFM does predict failure stemming from the hole to occur at higher loadings than those required to break a plain domain, thus “foreseeing” structural strengthening by material removal. This counterintuitive behavior arises from the interaction of the FFM stress condition, dominant for vanishing hole sizes, with the presence of a positive local minimum in  $\sigma_{\theta\theta}(r)$  for sub-zero  $\beta'$  values (case A5, see Table 1 and Fig. 2), which “shields” the triggering of failure when the failure initiation region represented by  $\Delta_f$  goes beyond a critical value. In turn, the fact that this only occurs for very small holes is a consequence of the size-effect that results from the stress and energy criterion being proportional to  $R$  and  $\sqrt{R}$ , respectively. Indeed, as  $R/l_{ch} \rightarrow 0$ , FFM's failure predictions associated with a crack stemming from the hole do not tend to the expectable  $\Sigma'_1 = \sqrt{2} \sigma_c / (1 + \beta')$  loading locus, but to that in Eq. (16) instead. In any case, this feature is an artifact of the straightforward application of the FFM approach to cracks stemming radially from a circular hole that presents no physical relevance: in those cases, failure triggers at infinity once the crack opening stress reaches  $\sigma_c$  therein, regardless of the presence of the hole, as reported in Fig. 3.

$$\frac{\Sigma'_1}{\sigma_c} = \begin{cases} \frac{\sqrt{2}}{1 + \beta' - \beta'^2/12} & \text{if } \beta' \leq 0 \\ \frac{\sqrt{2}}{1 + \beta'} & \text{if } \beta' > 0 \end{cases} \quad (16)$$

Interestingly, this issue does not affect the FFM-avg variant for it inherently considers the trivial no-hole solution in the failure load minimization procedure as aforementioned, thus predicting failure to asymptotically tend to  $\Sigma'_1 = \sqrt{2} \sigma_c / (1 + \beta')$  when  $R/l_{ch} \rightarrow 0$ , as also shown in Fig. 3.

Additionally, the presence of local extrema in  $K_I$  (and also in  $\tilde{K}_I$ ) for certain biaxiality conditions results in a very particular effect on both FFM and FFM-avg predictions: for a given hole size, there exists a critical

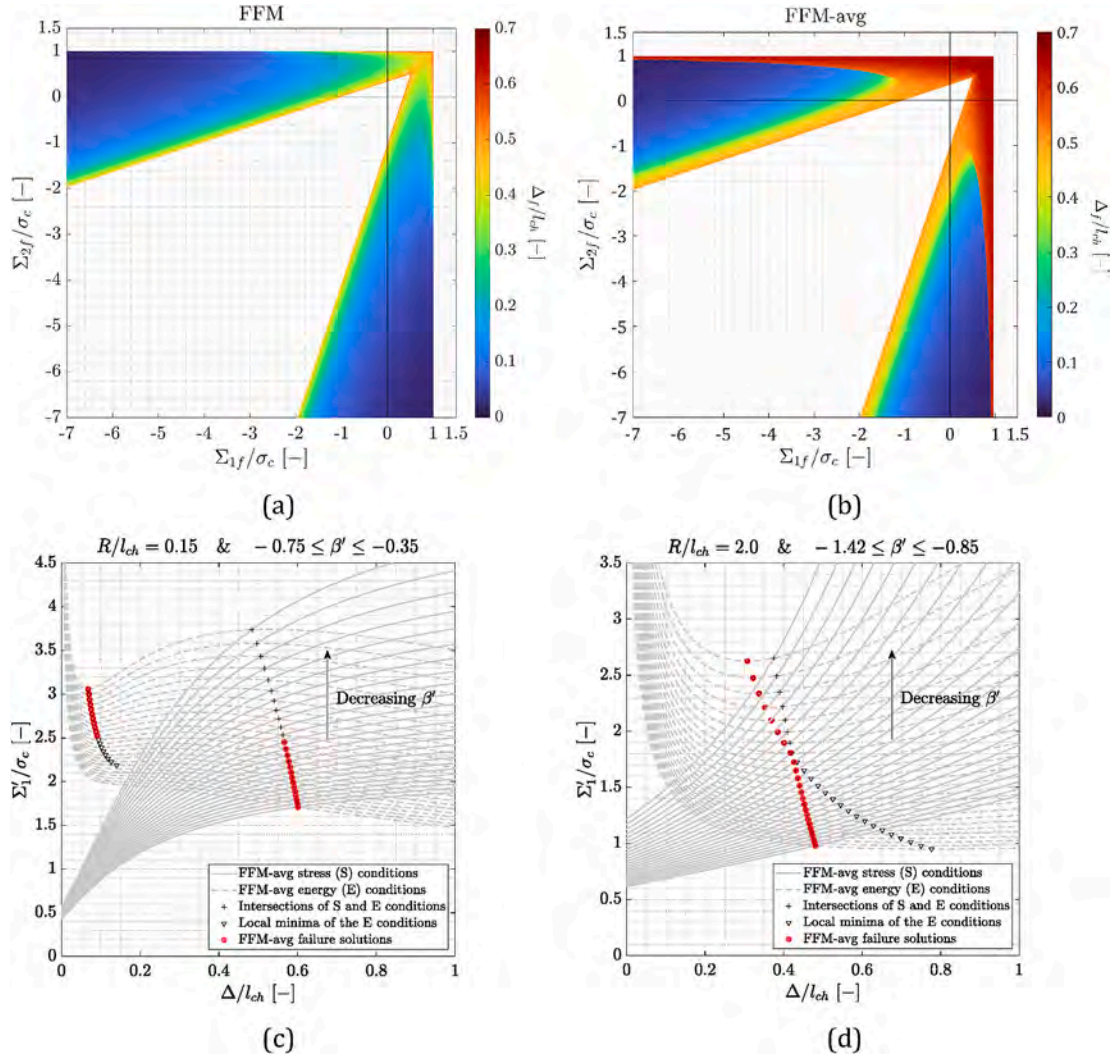


**Fig. 4.** Evolution of the critical length  $\Delta_f$  along the failure domain as predicted by FFM (a) and FFM-avg (b); and in the surroundings of the FFM-avg's Scenario C and E frontier for a small (c) and a large (d) hole, with  $\beta'$  as a parameter.

value of  $\beta'$  below which the crack onset stops occurring when both stress and energy inequalities become equalities (coupled scenario, C), and instead takes place at the minimum of the energy condition (energy scenario, E). This means that within the Scenario E, failure onset is predicted to be independent of the strength  $\sigma_C$  beyond its effect on the  $R/l_{ch}$  ratio. Furthermore, this implies that despite the non-singular geometry, failure might still be predicted as solely governed by the fracture toughness. Clearly, for a hole size and loading scenario in which both FFM and FFM-avg simultaneously predict failure within the E scenario, both failure predictions are identical. Remarkably, this predicted dual behavior was already noticed by Mantić (2009) for interfacial crack onset around cylindrical inclusions.

At the same time, the safety domains predicted by both Finite Fracture Mechanics approaches present one peculiar feature concerning the hole size-effect on failure: whereas the safety domains respective to the extreme cases ( $R/l_{ch} = 0$  and  $R/l_{ch} = \infty$ ) are mostly straight, the transition from one to another takes place through arched curves. This difference can be attributed to the fact that the extreme solutions are stress-dominated scenarios, whereas in the intermediate cases the energy balance also plays an important, or even dominant, role. Accordingly, the use of pure stress-based failure criteria, such as the Theory of Critical Distances (Taylor, 2007), would always yield failure domains that are straight in the loading space. This feature is clearly observed in Eq. (17), which results from the particularization for the case under study of the

Point Method of the Theory of Critical Distances.

$$\begin{aligned} \Sigma_{1f} \left[ 2 + \left( \frac{2\pi R}{2\pi R + l_{ch}} \right)^2 + 3 \left( \frac{2\pi R}{2\pi R + l_{ch}} \right)^4 \right] \\ + \Sigma_{2f} \left[ \left( \frac{2\pi R}{2\pi R + l_{ch}} \right)^2 - 3 \left( \frac{2\pi R}{2\pi R + l_{ch}} \right)^4 \right] = 2\sigma_C \end{aligned} \quad (17)$$

Furthermore, as previously mentioned, the coupling of stress and energy conditions also provides Finite Fracture Mechanics with an intrinsic definition of the structural length  $\Delta$  used to nonlocally assess the criterion, in turn rendering it very robust. Indeed, the interplay between the critical length  $\Delta_f$  and the structure itself results of special importance for the scenario here studied, given that the strict positivity of both the stress field and SIF functions is not always ensured in the prospective failure region. In this sense, Fig. 4 (a) and (b) illustrate the dependence that  $\Delta_f$  has with respect to the hole radius and the biaxial loading state for Finite Fracture Mechanics formulations. There should be noted that the dependence with the hole radius in Fig. 4 (a) and (b) is implicit, for one should first refer to either Fig. 3 (a) or (c) to determine the failure state ( $\Sigma_{1f} - \Sigma_{2f}$ ) predicted by either FFM or FFM-avg for the hole size and biaxiality ratio of interest, and then use the failure state to enter in Fig. 4 and get the corresponding value of  $\Delta_f$ . Given the above, there can be stated that  $\Delta_f$  presents a rather complex evolution all along the failure domain:  $\Delta_f$  is predicted to be larger towards the bi-traction

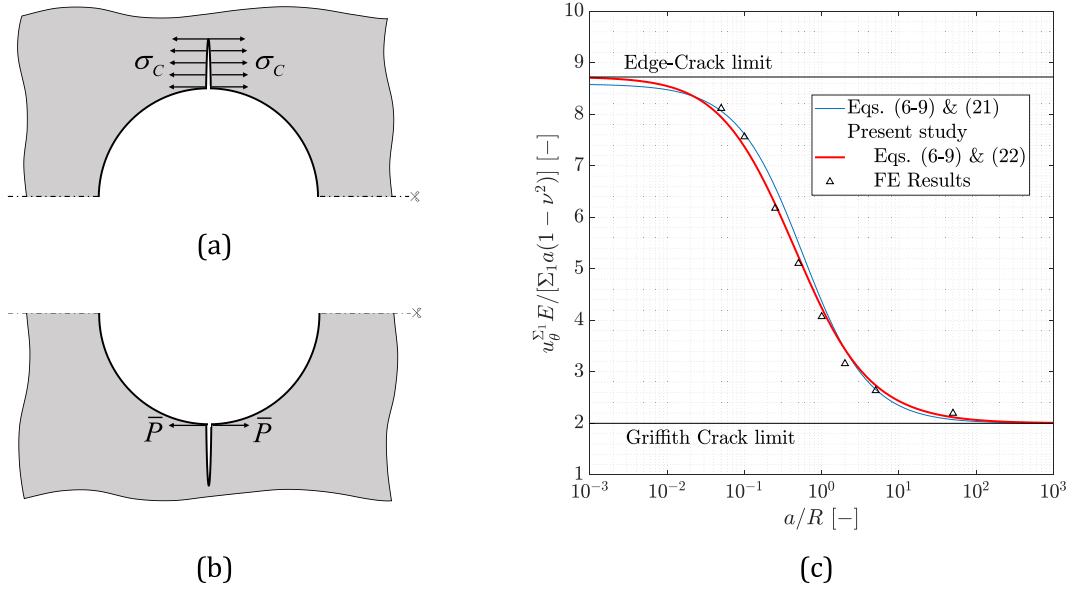


**Fig. 5.** Schematic representations of the CSL (a) and LLE (b) auxiliary loading scenarios; (c) Comparison of the CMOD values from approximating expressions and FE analyses for  $\beta' = 1$ .

loading states regardless of the used Finite Fracture Mechanics formulation, whereas Scenario E failures have an associated  $\Delta_f$  that tends to be lower than those in Scenario C. Remarkably, the latter feature is in agreement with what observed by Mantić (2009) for the delamination of inclusions. Likewise, Scenario C to E frontiers depicted in Fig. 3 (b), (d) and (e) are also embodied in Fig. 4 (a) and (b), which in turn show that this transition takes place as a discontinuity in  $\Delta_f$  for holes small enough, otherwise being continuous but not smooth. Likewise, this particularity of the Finite Fracture Mechanics approach is shown to be the most evident for the case of the FFM-avg.

A detailed analysis on the evolution and interplay of the FFM-avg stress and energy conditions is also conducted in Fig. 4 (c) and (d). In particular, these figures regard the cases of small and large holes, respectively, and therein  $\beta'$  is considered as a varying parameter. For both configurations, it is confirmed that the FFM-avg solution lies within Scenario C for relatively large values of  $\beta'$ , and within Scenario E for sufficiently negative  $\beta'$  values. Furthermore, these figures explicitly show the interplay between the local minimum of the energy condition (whenever it exists) and the intersection between the stress and energy condition, a fundamental difference between both cases being found. For the small hole, the locus of local minima of the energy condition and that of intersections between stress and energy conditions never cross as  $\beta'$  gets smaller, and so, the eventual transition from Scenario C to E can only materialize as a jump in  $\Delta_f$ . On the other hand, for the large hole configuration the locus of local minima of the energy condition and that of the Intersections of stress and energy conditions eventually cross as  $\beta'$  reduces, meaning that the transition from Scenario C to E is continuous in  $\Delta_f$ , although not smooth. Consequently, keeping constant the critical length used to non-locally assess the failure criterion would result in its inability to capture such complex dependences, the subsequent predictions being rendered meaningless for some loading configurations in the studied structural setup.

#### 4. Cohesive Zone Model

Once seen in the previous section the advantages arising from coupling stress and energy considerations upon failure onset predictions, there must be recalled that Finite Fracture Mechanics shares this feature with another well-established formulation: the Cohesive

Zone Model. Indeed, it is mainly the latter's merit that both the strength and the fracture energy started being simultaneously considered to model material failure. Nonetheless, the formulation of the Cohesive Zone Model is not unique for there exists many variants depending upon practical needs. They all agree to hypothesize that once reached the material strength, the continuum is no longer governed by a stress-strain relation, but by a stress-opening one. In turn, the definition of this latter relation, also denominated traction-separation law, is what gives Cohesive Zone Model its wide diversity by dictating how the continuum softens and builds up energy release upon damage evolution. In this sense, the region showcasing the cohesive behavior commonly receives the name of process zone. Eventually, failure initiation occurs as soon as the critical energy release threshold is reached within the process zone.

Aiming to provide the failure initiation predictions by a Cohesive Zone Model yet keeping its study analytical, the present work will only implement Dugdale's formulation (Dugdale, 1960), hereinafter referred to as CZM. Its simplicity lies in that once the material reaches its strength  $\sigma_c$ , a process zone will form in the prospective crack path, wherein the cohesive stress remains equal to  $\sigma_c$  regardless of the displacement jump thereof. This is maintained as the load increases up to the point in which the Crack Mouth Opening Displacement (CMOD –  $u_{\theta}$ ) reaches the critical value  $u_{\theta,c} = G_c/\sigma_c$ , instant in which the energy dissipated at the crack onset point overcomes the material fracture energy  $G_c$ , thus triggering failure.

As shown in Cornetti and Sapora (2019), the CZM can be implemented through a system of two equations with two unknowns, viz. the failure load  $\Sigma'_{lf}$  and the length of the process zone at failure  $a_{pf}$ . The first equation imposes that the SIF at the tip of the process zone (the *fictitious* crack tip, herein  $r = R + a_p$ ) is null as for the non-diverging stresses, whereas the second requires the displacement jump at the crack tip (the *real* crack tip, herein  $r = R$ ) be equal to  $G_c/\sigma_c$ . Noteworthy, as proposed in Chao Correias et al. (2021), the use of the Paris' integral introduced in Paris (1957) allows to write CZM's system of equations by means of just three SIF functions, corresponding to three loading cases: that under study plus two auxiliary ones, namely Constant Stress Lip (CSL) and Line-Load Edge (LLE) loadings. These latter two cases are schematically depicted in Fig. 5 (a) and (b), respectively.

Therefore, the SIF expression corresponding to symmetric antipodal radial cracks stemming from a circular hole under both CSL and LLE loading conditions are herein required besides that already reported in



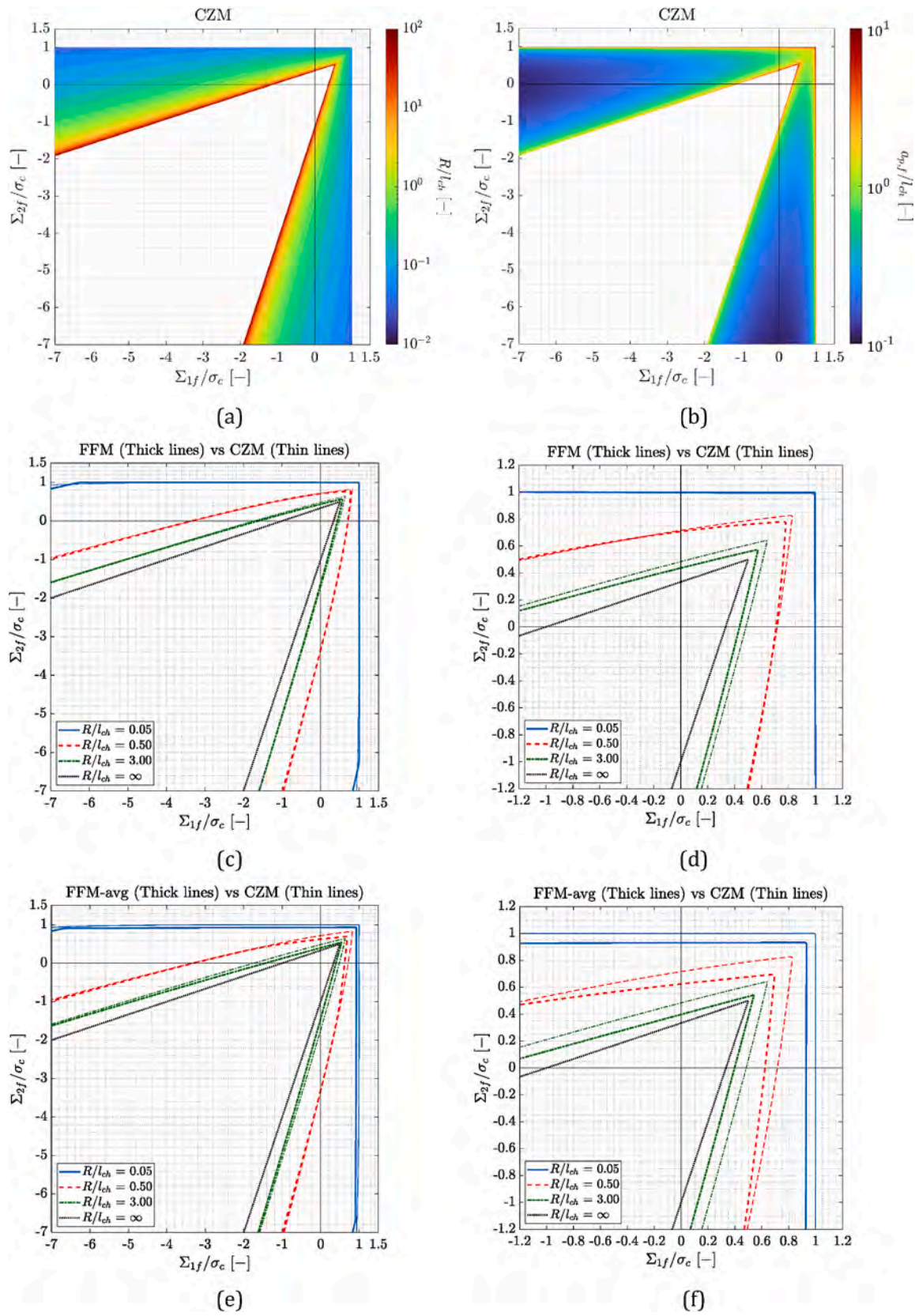


**Fig. 6.** Solution provided by CZM: safety domains (a) and evolution of  $a_{pf}$  (b); Comparison between the safety domains predicted by CZM and FFM (c, d), and by CZM and FFM-avg (e, f).



Section 2.2. For the CSL case, Tada et al. (2000) proposed the expression in Eqs. (18) and (19) which casts an error of less than 1%.

$$K_I^{\sigma_c}(a, \sigma_c) = \sigma_c \sqrt{\pi a} F^{\sigma_c}(a) \quad (18)$$

$$F^{\sigma_c}(a) = 1 + (1 - \xi) [-0.137 + 0.258(1 - \xi)^2 - 0.4\xi^2(1 - \xi)] \quad (19)$$

On the other hand, a proposal of the SIF expression for the LLE case was given in Williams et al. (2011) and herein reported in Eqs. (20) and (21).

$$K_I^{\bar{P}}(a, \bar{P}) = \frac{\bar{P}}{\sqrt{\pi a}} F_A^{\bar{P}}(a) \quad (20)$$

$$F_A^{\bar{P}}(a) = \frac{2\sqrt{R+a}}{\sqrt{2R+a}} \left[ 1 + 0.201 \left( \frac{R}{R+a} \right)^2 + 0.604 \left( \frac{R}{R+a} \right)^4 \right] \quad (21)$$

In like manner to what done in Chao Correias et al. (2021), the accuracy of the SIF shape function  $F_A^{\bar{P}}(a)$  was checked against Finite Element results. In particular, Fig. 5 (c) reports the results for the normalized CMOD ( $u_0^{\Sigma_1} E / [\Sigma_1 a (1 - \nu^2)]$ ;  $u_0^{\Sigma_1}$  being the CMOD) under uniaxial tensile loading conditions, i.e.  $\Sigma_1 > \Sigma_2 = 0$ . Indeed, there can be seen that despite the showcased overall good performance of  $F_A^{\bar{P}}$  with respect to FE results, it fails to yield the expected solution for the  $a \rightarrow 0$  limit case. Due to this, a new SIF shape function for the LLE case is proposed in Eq. (22), so that the extreme solutions, i.e.  $a \rightarrow 0$  and  $a \rightarrow \infty$ , are perfectly fulfilled, while the intermediate solutions are obtained through a proper interpolation function. Subsequently, it is seen in Fig. 5 (c) that the proposed SIF shape function  $F^{\bar{P}}(a)$  improves the accuracy to Finite Element results with respect to  $F_A^{\bar{P}}(a)$ , and thus the former will be used onwards.

$$F^{\bar{P}}(a) = 2.594 \left( \frac{R}{R+5a} \right)^2 + 2 \left[ 1 - \left( \frac{R}{R+5a} \right)^2 \right] \quad (22)$$

Therefore, the resultant system of two equations that governs the CZM solution is as given in Eq. (23): the first imposes null SIF at the tip of the process zone, whereas the second accounts for the energetic condition upon failure initiation.

$$\begin{cases} \frac{\Sigma'_{lf}}{\sigma_c} = \frac{F^{\sigma_c}(a_{pf})}{F_{\beta'}(a_{pf}, \beta')} \\ \Sigma'_{lf} = \frac{l_{ch} + 2 \int_0^{a_{pf}} F^{\sigma_c}(a) F^{\bar{P}}(a) da}{2 \int_0^{a_{pf}} F_{\beta'}(a, \beta') F^{\bar{P}}(a) da} \end{cases} \quad (23)$$

Remarkably, solving the system in Eq. (23) is equivalent to imposing the first order minimality condition on the failure load with respect to the process zone length in the second equation of Eq. (23) (see Annex A). Hereafter, equaling the right-hand side of both equalities in Eq. (23), the length of the process zone at failure  $a_{pf}$  can be directly determined from Eq. (24).

$$F^{\sigma_c}(a_{pf}) \int_0^{a_{pf}} F_{\beta'}(a, \beta') F^{\bar{P}}(a) da - F_{\beta'}(a_{pf}, \beta') \left( \frac{l_{ch}}{2} + \int_0^{a_{pf}} F^{\sigma_c}(a) F^{\bar{P}}(a) da \right) = 0 \quad (24)$$

Then, one can determine the weakening ratio  $\Sigma'_{lf}/\sigma_c$  by just inputting  $a_{pf}$  on either one of the equalities in Eq. (23). Clearly, Eq. (24) allows for fast and robust numerical obtention of the CZM failure predictions. Noteworthy,  $\Sigma'_{lf}/\sigma_c = \beta' \Sigma'_{lf}/\sigma_c$ .

Eventually, the CZM failure initiation predictions are reported as a contour map in Fig. 6 (a). Just like what observed in the Finite Fracture Mechanics predictions, CZM's safety domains are straight for extreme hole sizes ( $R \rightarrow 0$  and  $R \rightarrow \infty$ ) for being stress-dominated conditions, while for intermediate hole sizes the increasing importance of energy considerations forces them to curve. Likewise, the evolution of the process zone length at crack onset  $a_{pf}$  all along the failure domain is depicted in Fig. 6 (b). Therein, it is observed that diminishing the hole size entails the divergence of  $a_{pf}$  irrespective of  $\beta'$  due to the lose of importance of the stress concentration in the failure onset. Otherwise, it results that the evolution of CZM's  $a_{pf}$  is qualitatively equivalent to that of FFM's  $\Delta_f$  in Fig. 4 (a), in the sense that both  $a_{pf}$  and  $\Delta_f$  are large for high values of  $\beta'$  and diminish as the latter reduces.

Similarities in the predictions by FFM and CZM are clear from the comparisons shown in Fig. 6 (c) and (d), although the correlation between both varies with the biaxiality of the loading and the size of the hole. Clearly, the agreement for large hole sizes is almost perfect, whereas the solutions for smaller hole sizes present some differences, mainly due to FFM being exclusively governed by the energy condition for certain traction-compression load combinations. Concurrently, if the focus is set to hole radii other than the limit cases, there is revealed an interesting correlation between the closeness of FFM and CZM predictions and the maximum value of  $\sigma_{\theta\theta}$  in the domain at the instant of failure. The latter is represented in its normalized form by  $\hat{\sigma}_{\theta\theta f}$  and defined in Eq. (25).

$$\hat{\sigma}_{\theta\theta f} = \frac{\sigma_{\theta\theta}(r, \theta, \Sigma'_{lf}, \beta')|_{r=R, \theta=0}}{\sigma_c} = \frac{\Sigma'_{lf}}{\sigma_c} (\sqrt{2}\beta' + 2\sqrt{2}) \quad (25)$$

Indeed, as shown in Fig. 7, larger  $\hat{\sigma}_{\theta\theta f}$  values take place where the agreement between FFM and CZM predictions from Fig. 6 (c) and (d) improves. Analogous behaviors were reported in the literature: Cornetti and Sapora (2019) found that for a uniaxially tensioned Penny-shaped crack ( $\hat{\sigma}_{\theta\theta f} = \infty$ ) FFM and CZM are very close. In contrast, Chao Correias et al. (2021) reported higher differences for the case of a spherical void under uniaxial tension ( $\hat{\sigma}_{\theta\theta f} \in [1, \sim 2]$ ). Noteworthy, this reasoning is found to only hold true for the cases in which FFM predicted failure within the Scenario C, otherwise the differences between FFM and CZM are considerable even for large values of  $\hat{\sigma}_{\theta\theta f}$ .

Lastly, the comparisons between FFM-avg and CZM are also given in Fig. 6 (e) and (f) for the sake of completeness. It is shown that being the FFM-avg more conservative than FFM, its difference with CZM is larger

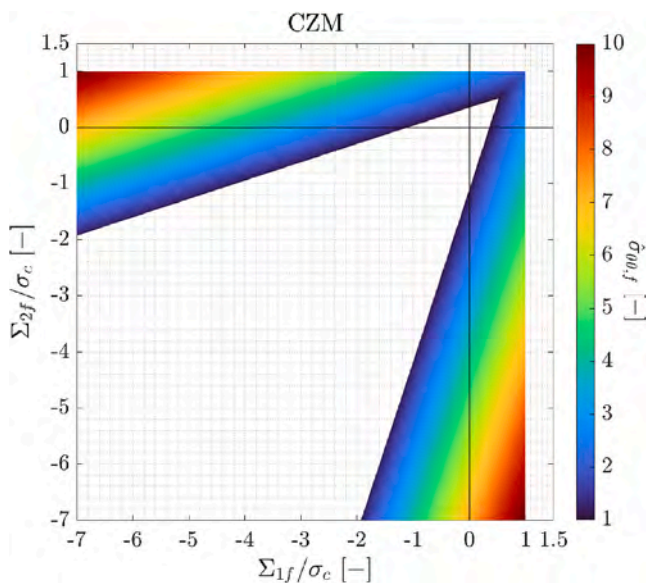


Fig. 7. Evolution of  $\hat{\sigma}_{\theta\theta f}$  according to CZM.

although both remain qualitatively similar. Notice that the discrepancies between FFM-avg and CZM failure predictions were already reported in the literature, for instance in [Cornetti and Sapora \(2019\)](#), [Chao Correias et al. \(2021\)](#) and [Ferrian et al. \(2022\)](#). A better match is usually expected between FFM-avg and the Cohesive Zone Model whenever linear softening is considered, as stated in [Cornetti et al. \(2019\)](#).

## 5. Phase Field model of fracture

The former two semianalytical methods herein used to address the crack initiation problem have proven to be robust, but they require the knowledge of the crack path beforehand. Additionally, the implementation of Finite Fracture Mechanics can be challenging, and it is mostly limited to relatively simple configurations in which analytical expressions for the stress field and SIF are available. Anyhow, the application of both Finite Fracture Mechanics (either FFM or FFM-avg) and CZM semi-analytical approaches was herein possible because these limitations do not show up for the case at hand. In turn, this renders the considered structural configuration a perfect benchmark to test the performance of more advanced failure models against those already well-settled in a wide range of failing conditions (see Section 2.3).

In this sense, the present Section will be devoted to the implementation of one of the frameworks that is attracting the largest share of attention among the fracture mechanics community: the Phase Field modelling of fracture ([Francfort and Marigo, 1998](#)). Added to a convenient numerical implementation and the absence of requiring *a priori* knowledge of the crack path, this approach represents a regularization of the Griffith problem in the sense of  $\Gamma$ -convergence ([Bourdin et al., 2008](#)), and so, it is adequate for use in complex crack propagation events. On the other hand, and despite the existent gaps of the theoretical background in what concerns its use for failure initiation problems (for which this approach works as a Gradient Damage Model), recent works have proven that it also has the potential to deliver predictions in reasonable agreement with FFM ([Molnár et al., 2020](#)) or with experiments ([De Lorenzis and Maurini, 2022](#)).

In the bigger picture, the Phase Field models of fracture differ from the Finite Fracture Mechanics and Cohesive Zone Model approaches in that they are entirely written in terms of energy and do not account for explicit stress conditions to capture failure. As a matter of fact, the former approach relies on seeking for the minimization of the total potential energy  $\Pi_{TOT}$  stored in the structural domain  $\Omega$  as defined in Eq. (26) for a quasi-static setup. Therein,  $\Pi_S$  and  $\Pi_F$  stand for the strain and fracture components of the potential energy, respectively, and  $\Pi_{EXT}$  represents the external work, although the latter will not be herein considered. To achieve so, the standard energetic formulation of the structural problem in terms of the displacement field  $\vec{u}(\vec{x})$  is enriched with an additional continuous scalar field, namely the damage variable  $\alpha(\vec{x})$ , that indicates whether a material is in pristine ( $\alpha = 0$ ), damaged ( $\alpha \in (0, 1)$ ) or fully broken ( $\alpha = 1$ ) conditions. To ensure that no “material healing” takes place, the damage variable is subjected to an irreversibility condition that precludes it from diminishing with respect to previous material states.

$$\Pi_{TOT}(\vec{u}, \alpha) = \Pi_S(\vec{u}, \alpha) + \Pi_F(\alpha, \vec{\nabla}\alpha) - \Pi_{EXT}(\vec{u}) \quad (26)$$

The actual choice of the  $\Pi_S(\vec{u}, \alpha)$  and  $\Pi_F(\alpha, \vec{\nabla}\alpha)$  functions depends on the considered Phase Field model of fracture and will be commented hereafter, but anyhow  $\Pi_S$  and  $\Pi_F$  must be monotonically decreasing and increasing with  $\alpha$ , respectively. At the same time, given that the Phase Field models of fracture fall within the category of Gradient Damage models, the dissipative term  $\Pi_F$  presents not only an explicit dependence with  $\alpha$  but also with its gradient  $\vec{\nabla}\alpha$ . Likewise,  $\Pi_F$  should also showcase a monotonically increasing dependence with  $\vec{\nabla}\alpha$ , implying that abrupt changes in the material state are energetically expensive. Therefore, the transition between pristine and broken material states is forced to take place continuously and within finite-size subdomains, whose dimension

is controlled by another key feature of the Phase Field model of fracture: the internal length  $\ell$ . Consequently, discontinuities in the material state, such as cracks, smear within the domain, thus easing the numerical treatment of the problem.

In what concerns to the specifics of the Phase Field formulation, the present work will only consider the so-called AT1 damage law (see e.g. ([De Lorenzis and Maurini, 2022](#))). Its main advantage with respect to the other most widespread Phase Field damage law –the AT2– is that the former allows for pure elastic behavior at sufficiently low stress levels while the latter does not ([Marigo et al., 2016](#)), in turn leading AT1 to better capturing the energy dissipation upon failure ([Bleyer et al., 2017](#)). This AT1 damage law gets defined by the two constitutive functions  $a_{PF}(\alpha)$  and  $w_{PF}(\alpha)$  given in Eqs. (27) and (28): the former modulates  $\Pi_S$  with the evolution of the damage, while the latter controls the local term of  $\Pi_F$ , i.e. the one depending on the local values of  $\alpha$ .

$$a_{PF}(\alpha) = (1 - \alpha)^2 \quad (27)$$

$$w_{PF}(\alpha) = \alpha \quad (28)$$

Likewise, the general definition of  $\Pi_F$  is given in Eq. (29), where  $c_w$  is defined in Eq. (30) and represents a scaling coefficient that enforces the specific energy released upon localized fracture of a uniaxial bar under tension to be  $G_C$ .

$$\Pi_F(\alpha, \vec{\nabla}\alpha) = \frac{G_C}{c_w} \int_{\Omega} \frac{w_{PF}(\alpha)}{\ell} + \ell (\vec{\nabla}\alpha \cdot \vec{\nabla}\alpha) \, d\vec{x} \quad (29)$$

$$c_w = 4 \int_0^1 \sqrt{w(\zeta)} \, d\zeta \quad (30)$$

As a result, there exists a competition between the local and non-local terms of  $\Pi_F$  in the transition from pristine to broken material states, since smoother evolutions mean larger  $\alpha(\vec{x})$  and smaller  $\vec{\nabla}\alpha(\vec{x})$  values along the domain  $\Omega$ , and vice versa. Indeed, it is the internal length  $\ell$  the parameter that governs the relative importance of each contribution: larger (smaller) values of  $\ell$  increases (reduces) the energetic importance of the non-local term, smoothening (sharpening) these transitions.

The last ingredient required for the implementation of the Phase Field model of fracture is thus the definition of  $\Pi_S$ . Being this energy term the one controlling how the material model gets its strain energy component affected as the damage develops, a wide range of proposals, the so-called energy decompositions, exists in the literature (see ([De Lorenzis and Maurini, 2022](#))). In particular, two of the most relevant models will be presented in the following subsections: the first one due to its simplicity, the second due to its potential applicability to brittle materials only damageable in tension.

### 5.1. No decomposition (PF-NoSplit)

The most basic choice for the strain energy term within the framework of linear elasticity consists in not performing any energy decomposition and, thus, assuming that all the components of the deformation are equally affected by the damage development. This results into the expression in Eq. (31), where  $\psi_0$  represents the common linear elastic energy density function defined in Eq. (32),  $\bar{\epsilon}(\vec{u})$  is the infinitesimal strain tensor associated to the displacement field  $\vec{u}$ , and  $\lambda$  and  $\mu$  are the Lamé constants.

$$\Pi_S^{NS}(\vec{u}, \alpha) = \int_{\Omega} a_{PF}(\alpha) \psi_0(\bar{\epsilon}(\vec{u})) \, d\vec{x} \quad (31)$$

$$\psi_0(\bar{\epsilon}(\vec{u})) = \frac{\lambda}{2} \text{tr}(\bar{\epsilon}(\vec{u}))^2 + \mu(\bar{\epsilon}(\vec{u}) : \bar{\epsilon}(\vec{u})) \quad (32)$$

As a consequence, the resultant failure-wise behavior is symmetric, in the sense that both tensile and compressive stress states trigger the

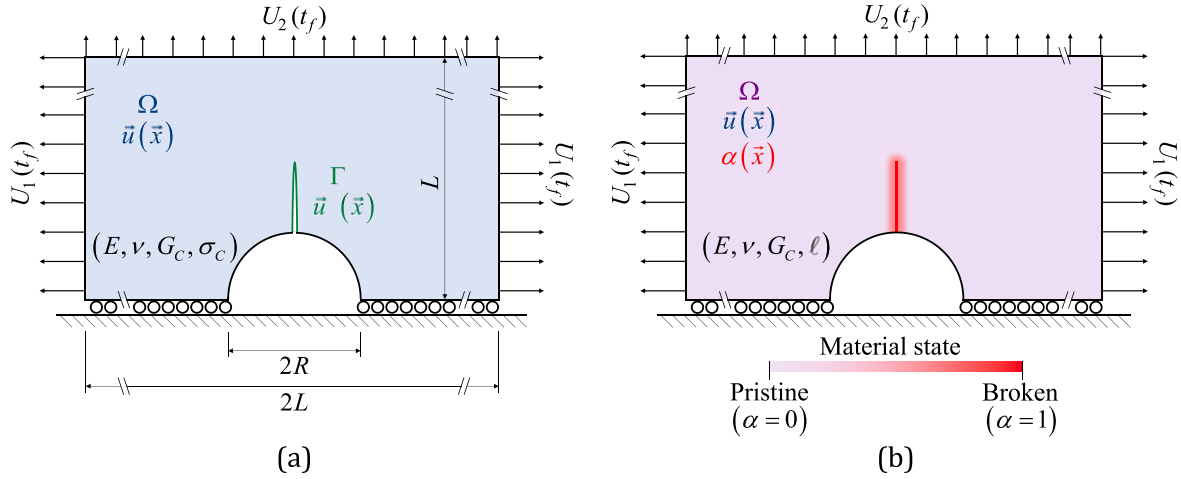


**Fig. 8.** Failure initiation problem in a sufficiently large domain containing a circular hole under biaxial loading: Schematic descriptions of the actual failure event (a) and of the Phase Field approximation (b).

same damage response at equal absolute stress values. Anyhow, and despite this symmetric failure envelope not being in accordance with most of the documented ultimate material behaviors, the model's simplicity and reasonable performance for fracture occurring in tensile-dominated structures makes it still widely implemented.

Subsequently, should the PF-NoSplit model be implemented for the case of a plain slab in plane strain conditions and under biaxial loading, akin to the scenario in Fig. 8 (a) when  $R \rightarrow 0$ , one can determine that the stress level  $\Sigma'_{1f}(\beta') \Big|_{R \rightarrow 0}^{NS}$  at which the failure onset takes place follows Eq. (33), where it still holds that  $\Sigma'_{2f}/\sigma_C = \beta' \Sigma'_{1f}/\sigma_C$ .

$$\Sigma'_{1f}(\beta') \Big|_{R \rightarrow 0}^{NS} = \sqrt{\frac{3 G_C E}{8 \nu (1 + \nu)}} \frac{1}{1 + (1 - 2\nu) \beta'^2} \quad (33)$$

Then, particularizing Eq. (33) for  $\beta' = 1$  and converting the obtained  $\Sigma'_{1f}$  and  $\Sigma'_{2f}$  dyad back to the baseline loading space as per Eq. (1), one gets the equivalent uniaxial tensile strength yielded by this Phase Field model of fracture, which results to be  $\sigma_C^{NS} = \sqrt{3 G_C E / [8 \nu (1 - \nu^2)]}$ .

## 5.2. No-tension decomposition (PF-NoTension)

The unrealistic symmetric failure behavior obtained from the previous definition of the strain energy poses a great setback to address fracture in scenarios where both tensile and compressive stress regions lie within the prospective crack path. Therefore, more advanced energy decompositions are required. In this regard, a very promising proposal was made by Freddi and Royer-Carfagni (2010), which, on the basis of the theory of structured deformations (Del Piero and Owen, 1993), aimed at introducing a strain energy function that would mimic the so-called No-Tension materials once the continuum gets fully damaged. To accomplish that, inelastic “structured deformations”, represented by  $\bar{\eta}(\bar{u})$ , were introduced in the formulation so that they reduce the actual strain energy of the domain as the material gets damaged, in a similar way micro-cracking events affect tensioned materials in reality. Specifically for the no-tension model, the inelastic deformations ought to

comprise all the strain components related to tensile states, i.e. those activating the opening of microcracks. In view of this,  $\bar{\eta}(\bar{u})$  gets defined as the second order tensor belonging to the set of symmetric and semi-definite positive tensors ( $\varphi \in \text{Sym}^+$ ) that maximizes the reduction of the resultant “elastic” strain energy, as given in Eq. (34).

$$\bar{\eta}(\bar{u}) = \underset{\bar{\varphi} \in \text{Sym}^+}{\text{argmin}} (\psi_0(\bar{\varepsilon}(\bar{u}) - \bar{\varphi})) \quad (34)$$

Although minimization problems are generally difficult to solve, it was proven in Sacco (1990) that both  $\bar{\varepsilon}(\bar{u})$  and  $\bar{\eta}(\bar{u})$  tensors are coaxial when linear elastic and isotropic materials are considered, meaning that these two second order tensors admit a shared base of eigenvectors. Consequently, the otherwise complex minimization problem in Eq. (34) rather simplifies and becomes analytically solvable in terms of the respective sets of eigenvalues of  $\bar{\varepsilon}(\bar{u})$  and  $\bar{\eta}(\bar{u})$ . Henceforth, and given the here considered plane strain conditions, there will be assumed without any loss of generality that the eigenvalues of both the infinitesimal and structured deformation tensors follow  $(\cdot)_I \geq (\cdot)_{II}$ , eventually yielding the definition of  $\bar{\eta}(\bar{u})$  in Eq. (35).

$$[\eta_I, \eta_{II}] = \begin{cases} [0, 0] & \text{if } (1 - \nu)\varepsilon_I + \varepsilon_{II} \leq 0 \\ \left[ \varepsilon_I + \frac{\nu}{1 - \nu}\varepsilon_{II}, 0 \right] & \text{if } (1 - \nu)\varepsilon_I + \varepsilon_{II} > 0 \text{ and } \varepsilon_{II} < 0 \\ [\varepsilon_I, \varepsilon_{II}] & \text{if } \varepsilon_{II} \geq 0 \end{cases} \quad (35)$$

The resultant definition of the strain energy component as per the PF-NoTension decomposition given in Eq. (36) was introduced in De Lorenzis and Maurini (2022) as the generalization for any proper  $a_{PF}(\alpha)$  function of the original proposal by Freddi and Royer-Carfagni (2010).

$$\Pi_s^{NT}(\bar{u}, \alpha) = \int_{\Omega} \psi_0 \left( \bar{\varepsilon}(\bar{u}) - \left( 1 - \sqrt{a_{PF}(\alpha)} \right) \bar{\eta}(\bar{u}) \right) d\bar{x} \quad (36)$$

Therefore, according to Eqs. (35) and (36), only when the domain is subjected to a certain tensile state, i.e.  $\bar{\eta}(\bar{u}) \neq 0$ , the effect of the damage field on  $\Pi_s^{NT}$  is not cancelled out, and, thus,  $\alpha(\bar{x})$  can develop. In turn, this also implies that the material model keeps intact its stiffness

**Table 2**

Material properties and modelling parameters used for the Phase Field simulations.

$E$ , MPa	$\nu$ , [-]	$G_C$ , MPa·mm	$\ell$ , mm	$\sigma_C^{NS}$ , MPa	$\ell_{ch}^{NS}$ , mm	$\sigma_C^{NT}$ , MPa	$\ell_{ch}^{NT}$ , mm
2300	0.3	0.461	0.025	132.20	0.067	146.32	0.054

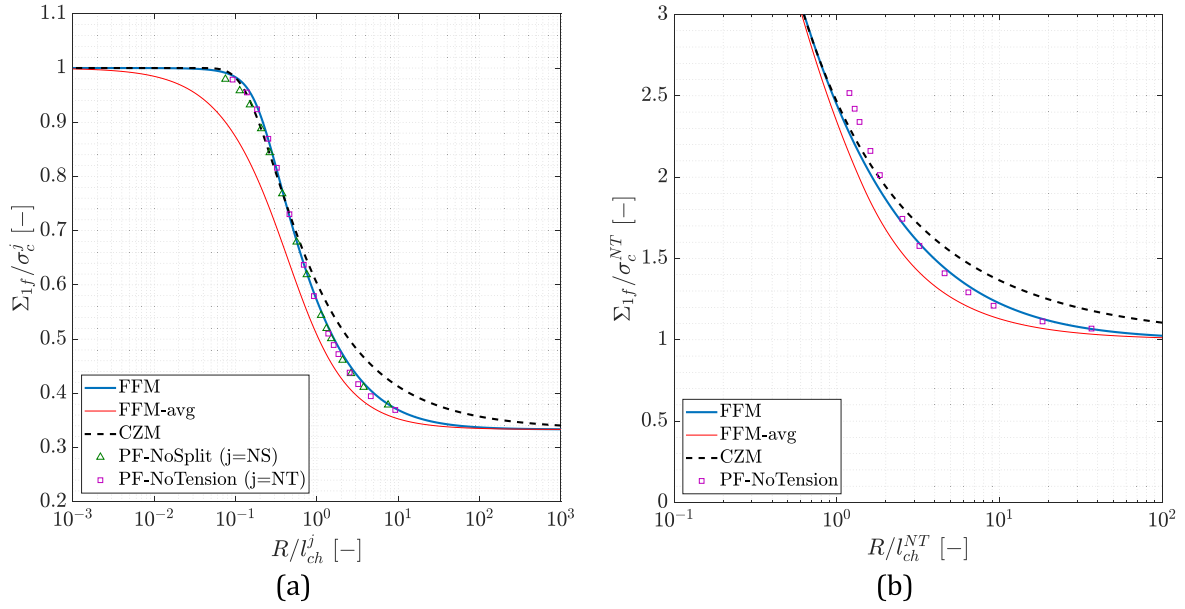


Fig. 9. Size-effect of failure for uniaxial tension (a) and uniaxial compression (b).

under compressive stress states even when fully broken ( $\alpha = 1$ ), mimicking the contact between the crack lips under compression and avoiding interpenetration. Indeed, Eq. (36) implies that the damage variable  $\alpha$  acts as a modulator of the magnitude that  $\Pi_s^{NT}$  reduces due to  $\bar{\eta}$ , which in turn does not explicitly depend on the damage. In this sense, the present model states that pristine materials ( $\alpha = 0$ ) are not affected at all by inelastic deformations, whereas the effect of  $\bar{\eta}$  gradually increases with  $\alpha$  until it is total for fully broken conditions ( $\alpha = 1$ ). On the other hand, for sufficiently tensile conditions, viz.  $\bar{\eta}(\bar{\mathbf{u}}) = \bar{\varepsilon}(\bar{\mathbf{u}})$ , the strain energy component corresponding to the PF-NoSplit model in Eq. (31) is recovered, implying that all deformation components take part in the release of energy due to the damage evolution. Remarkably, the equivalence between PF-NoSplit and PF-NoTension formulations (and even others, see (De Lorenzis and Maurini, 2022)) is profound, since the former can be recovered from Eqs. (34) and (36) by changing the set of admissible structured deformations from  $Sym^+$  (symmetric and semi-definite positive tensors) to  $Sym$  (symmetric tensors).

Lastly, the respective stress level that triggers failure for the plain slab under biaxial loading conditions  $\Sigma'_{1f}(\beta')|_{R \rightarrow 0}^{NT}$  is obtained as per Eq. (37). Its definition shows the existence of two differentiated failure regimes: on one side,  $\Sigma'_{1f}(\beta')|_{R \rightarrow 0}^{NT}$  is equal to the function reported in Eq. (33) for sufficiently high values of  $\beta'$ ; on the other hand, once  $\beta'$  becomes smaller than  $1/(1 - 2\nu)$ , the solution tends to a vertical straight line in the baseline loading space  $(\Sigma_1 - \Sigma_2)$  so that  $\Sigma_{1f} = \sqrt{3 G_c E(1 - \nu)/[8\ell(1 + \nu)(1 - 2\nu)]}$ , which in addition coincides with the value of the uniaxial tensile strength  $\sigma_c^{NT}$ . At the same time, no failure according to the PF-NoTension model is possible for  $\beta' < -1$  in a plain slab, i.e. for bi-compressive loadings, thus implying that the compressive stress states do not play any role in the occurring of fracture. As a result, the PF-NoTension energy decomposition is well-aligned with the hypothesis used for the above presented Finite Fracture Mechanics and Cohesive Zone Models.

$$\Sigma'_{1f}(\beta')|_{R \rightarrow 0}^{NT} = \begin{cases} \sqrt{\frac{3 G_c E}{8\ell(1 + \nu)} \frac{2(1 - \nu)}{(1 - 2\nu)(1 + \beta')^2}} & \text{if } -1 \leq \beta' \leq \frac{1}{1 - 2\nu} \\ \sqrt{\frac{3 G_c E}{8\ell(1 + \nu)} \frac{1}{1 + (1 - 2\nu)\beta'^2}} & \text{if } \frac{1}{1 - 2\nu} \leq \beta' \leq \infty \end{cases} \quad (37)$$

### 5.3. Implementation

In the present work, the different considered Phase Field models of fracture were implemented using the open source Finite Element computing platform FEniCSx, which is the latest version of the FEniCS project (Alnæs et al., 2015). To that end, the original problem under study herein, i.e. that described in Fig. 1 (a), was adapted as schematically shown in Fig. 8. Geometrically, this consisted in relaxing the initial infiniteness of the plane strain domain to being sufficiently larger than the hole (at least  $L/R \sim 40$ ), as well as in only exploiting the horizontal plane of symmetry to minimize computational effort yet ensure that the prospective crack onset region  $\Gamma$  stays away of the modelled domain boundaries. Additionally, the original Neumann boundary conditions got substituted by Dirichlet ones to be able to cope with material softening once damage develops. In any case, the equivalent remote failure stresses  $\Sigma_{1f}$  and  $\Sigma_{2f}$  were computed out of the reaction forces at the “instant” of crack onset  $t_f$ . In order to ensure the proper discretization of the domain at a reasonable computational cost, the characteristic mesh size in the prospective failure region was set to  $\ell/7$ , while the rest of the domain was discretized with elements sized  $h \sim L/40$ .

Eventually, the resolution of the Phase Field problem was performed iteratively at two levels: the first one concerning the loading, which was gradually raised up to the “instant” of failure  $t_f$  in which  $\alpha$  got sufficiently developed anywhere within the domain meaning that failure initiation could be acknowledged; and the second one regarding the minimization of the Phase Field energy functional at each time step, which was performed through an alternate minimization staggered scheme with convergence control at each iteration.

For all the simulations hereafter presented, the input material properties and modelling parameters are provided in Table 2, which in turn mostly correspond to those used in Kumar et al. (2020) for PMMA. Likewise, the resultant values for the uniaxial strength  $\sigma_c$  and Irwin's



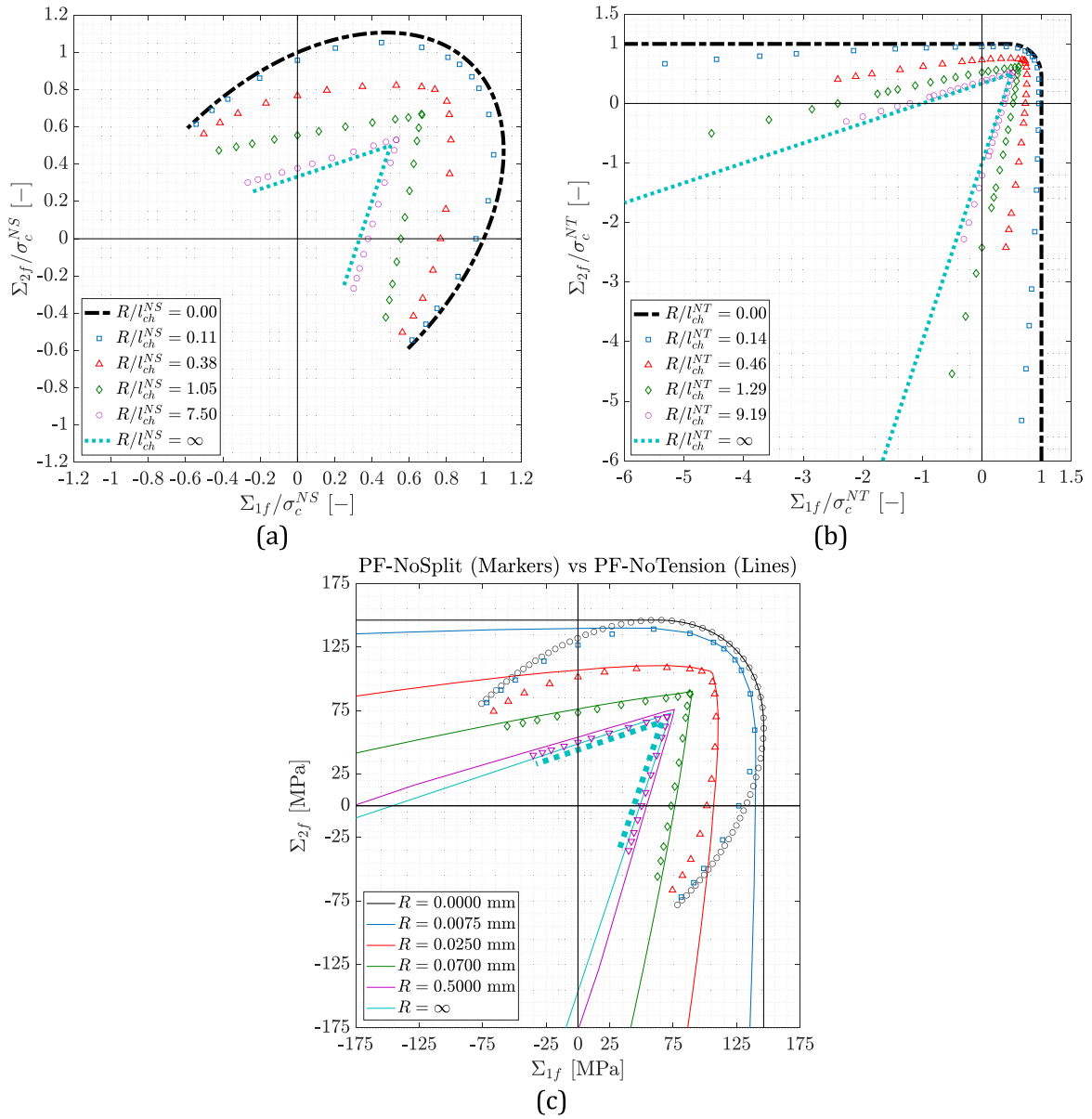


Fig. 10. Biaxial safety domains as per: PF-NoSplit (a), PF-NoTension (b), and both (c). Matching colors imply equal hole radius.

length  $l_{ch}$  for each energy decomposition used (NoSplit/NS and NoTension/NT) are therein given. It is noteworthy that the input properties and parameters of the Phase Field model of fracture, i.e.  $(E, \nu, G_C, \ell)$ , are herein kept constant for both formulations. This choice results into a model-dependent  $\sigma_c$ , which, on the other hand, should ideally be a material parameter. Nonetheless, it is deemed more coherent with the spirit of a regularized energy approach to fix the elastic properties  $E$  and  $\nu$ , the fracture toughness  $G_C$  and the internal length  $\ell$ . In any case, the meaningfulness of the safety domain comparison is ensured through proper failure stress normalization.

To first check whether the size-effect captured by the above defined Phase Field models of fracture are in accordance with the predictions of FFM, FFM-avg, and CZM, just the uniaxial tensile and compressive loading scenarios are addressed and reported in Fig. 9. Therein, the superindices in  $\sigma_c$  and  $l_{ch}$  respectively indicate the values used for normalizing the failure stress and hole radii of the Phase Field results. For the uniaxial tensile case in Fig. 9 (a), both Phase Field models perform almost identically and show great agreement with FFM. Interestingly, the observed correlation is better than that reported in Molnár

et al. (2020) for the Griffith crack.

For the uniaxial compression instead, the symmetric response to failure of the PF-NoSplit model invalidates its results as for predicting failure in compressed regions. Therefore, only the failure initiation predictions obtained from the PF-NoTension model are reported in Fig. 9 (b), where once again FFM is the approach providing the best agreement, especially for holes whose radius comply with  $R > 2l_{ch}^{NT}$ . Nonetheless, as the hole radius diminishes, the dimension of the tensile region ahead of the hole becomes of the order of magnitude of the internal length  $\ell$ , thus triggering a shielding effect that yields failure predictions considerably higher than those of the other three criteria. Eventually, for hole radii approximately smaller than  $l_{ch}^{NT}$ , the PF-NoTension failure onset predictions became unreliable for not being independent of the threshold of  $\alpha$  used for numerically assessing whether the material has failed or not, and so these are here omitted. In what concerns the crack arrest after initiation, both Phase Field models agree to predict unstable crack propagation for the uniaxial tensile case, while PF-NoTension did foresee the happening of the crack arrest after failure initiation in the uniaxial compressive scenario.

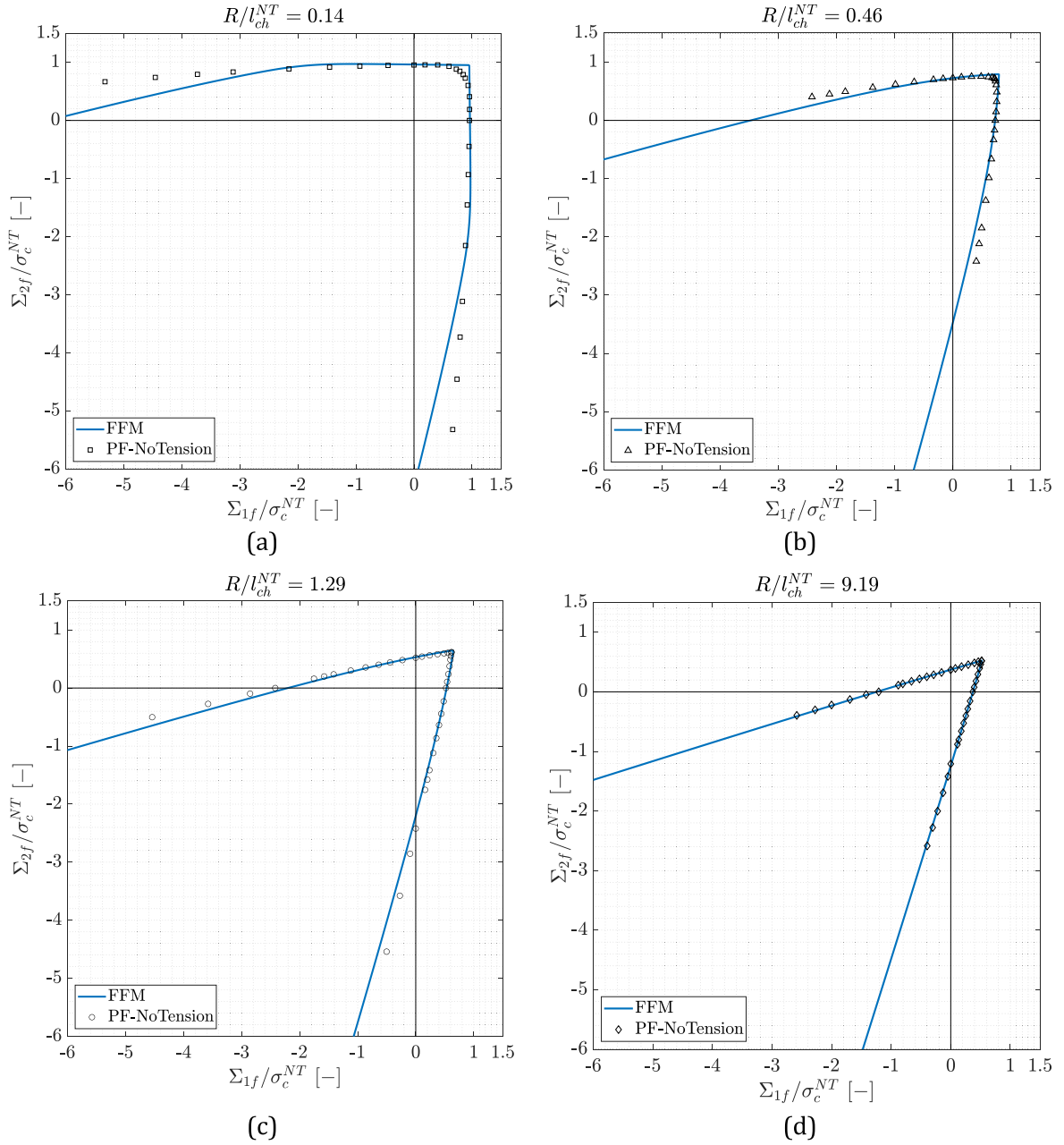


**Fig. 11.** Comparison of the biaxial safety domains by FFM and PF-NoTension for various hole radii.

Indeed, the similarities between both Phase Field formulations are mainly restricted to tensile-dominated failure conditions, as already expected from Eqs. (33) and (37), while compressive stress states are treated in a completely different manner. In this sense, their discrepancies become rather evident once the full biaxial loading scene is considered, as now shown in Fig. 10.

Results in Fig. 10 (a) corresponding to the failure domains predicted by PF-NoSplit show the tendency towards the elliptical safety domain given in Eq. (33) as the size of the hole vanishes. As the hole size gets larger, the rounded safety domains straightens, eventually tending to the same spear-shaped failure domain seen in all three previous criteria (FFM, FFM-avg and CZM). This arises from the large hole solution being only affected by the local values of the stress field at the point of failure onset, rendering it governed by the relation  $\hat{\sigma}_{\theta\theta} = 1$  (see Eq. (25)) due to  $\sigma_{rr}(r = R, \theta)$  being null. Consequently, and differently from Finite Fracture Mechanics and CZM, PF-NoSplit always predicts curved safety

domains, but for the cases where the holes are very large. Likewise, since every component of deformation is capable of dissipating fracture energy, the PF-NoSplit is not capable of predicting the happening of crack arrest in the case studied. In fact, and despite the crack patterns are out of the scope of the present work, it was noticed that, as the pure shear loading condition ( $\beta' \rightarrow 0$ ) was approached, dissipation through shear bands would take an increasingly important role through the appearance of  $\pm 45^\circ$  crack segments after failure onset. Noteworthy, as long as  $\beta'$  remained positive, the failure pattern would always initiate straightly at  $\theta = 0$ , but the length of the straight segment would vanish as  $\beta' \rightarrow 0$ . Consequently, only cases in which  $\beta' > 0$  are reported in Fig. 10 (a) since these were those in which failure initiated along the  $\theta = 0$  direction as initially hypothesized.

On the other hand, the safety domains obtained through the PF-NoTension show far better agreement with what obtained through the FFM, FFM-avg and CZM approaches, as shown in Fig. 10 (b). Indeed, by

only allowing deformations associated with tensile states to dissipate energy upon fracture, the failure initiation predictions become mostly straight as the hole size diminishes (see Eq. (37)), in line with the semianalytical approaches. For intermediate hole sizes, the safety domains show a certain curvature that eventually vanishes for the large hole solution, which once again is governed by the relation  $\hat{\sigma}_{\theta\theta} = 1$ . Likewise, the shielding effect already noticed in the uniaxial compressive case did also appear for the two lowest hole sizes considered, i.e.  $R/l_{ch}^{NT} = 0.14$  and  $R/l_{ch}^{NT} = 0.46$ . In both of them, failure initiation predictions turned unreliable once  $\beta'$  got smaller than approximately  $-0.7$ . Hence, this phenomenon cannot be explained as only arising from the presence of compressive stresses ahead of the hole since, according to the evolution of  $\sigma_{\theta\theta}(r)$  in Table 1, it is not until  $\beta' \approx -0.9$  that it becomes compressive at some point along  $\theta = 0$ . Instead, an alternative explanation can be given on the basis of the evolution of  $K_I(a)$ , which for  $\beta' < -0.194$  is no longer monotonically increasing. Therefore, the decreasing trait of  $K_I(a)$  can act as a halter of the failure initiation so that, should the local maximum be sufficiently close to the hole with respect to  $\ell$ , e.g. for very small holes, it would not let the failure initiation develop properly. In what concerns the crack onset patterns, PF-NoTension has revealed straight crack patterns in the  $\theta = 0$  radial direction for all hole sizes and loading biaxialities here considered, as opposed to the PF-NoSplit model. Even more so, for sufficiently negative values of  $\beta'$ , crack arrest after crack onset was observed, although careful analysis of such a matter falls out of the scope of the present work.

For a better comparison, the failure predictions from both PF-NoSplit and PF-NoTension models are superposed in Fig. 10 (c) in a dimensional fashion. There, both energy decompositions are shown to yield almost identical failure predictions for sufficiently large values of  $\beta'$  and small hole sizes. Nonetheless, the failure initiation predictions by both energy decompositions rapidly diverge as  $\beta'$  tends to 0 due to their respective discrepancies in how the compressive stress states affect the dissipation of fracture energy. At the same time, though qualitatively similar, the crack onset predictions for the large hole cases are quantitatively different. This is due to the large hole limit case ( $R \rightarrow \infty$ ) being governed by the relation in Eq. (38), in which the respective tensile strength measure  $\sigma_c^i$  ( $i = \{NS, NT\}$ ) is different for each energy decomposition. Therefore, since  $\sigma_c^{NT}$  is approximately 10% larger than  $\sigma_c^{NS}$ , the PF-NoTension failure onset predictions for the large hole limit case are slightly higher than those of PF-NoSplit, but with identical shape.

$$\sigma'_{lf}(\beta') = \frac{\sqrt{2}}{4 + 2\beta'} \sigma_c^i \quad (38)$$

Finally, it results interesting to investigate how well the Phase Field failure predictions compare with those of the above introduced models. In particular, given that the FFM and PF-NoTension have proven to generally be in good agreement for the uniaxial loading cases as per Fig. 9, only these two models are hereafter compared in Fig. 11. The correlation between both approaches in terms of the shape and size-effect of the safety domains is confirmed and noticeable discrepancies were only found for the smallest hole radius under study (see Fig. 11 (a)). For that case, the safety domains predicted by both approaches showed an increasing difference as the FFM's failure predictions fell deeper within the respective Scenario E of failure (see Fig. 3 (b)), thus inferring that their excellent agreement mostly holds for the cases dominated by the coupled criterion, i.e. Scenario C. Likewise, since the FFM failure criterion considers a Rankine-like stress condition purely written in terms of just  $\sigma_{\theta\theta}$ , it is unable to capture any biaxiality effect for the small hole limit case ( $R \rightarrow 0$ ) as clearly seen in the first quadrant of Fig. 11 (a). On the other hand, PF-NoTension predicts certain biaxiality effect for small holes and large values of  $\beta'$ , in turn more aligned with the results of relevant experimental campaigns, as those reported in De Lorenzis and Maurini (2022). As a result, there can be concluded that, despite being two failure criteria substantially different, FFM and

PF-NoTension are both qualitatively and quantitatively in agreement to a large extent in what concerns the predicted safety domains. Nonetheless, an even better agreement could be achieved by modifying the Rankine-like stress condition within the Finite Fracture Mechanics framework to account for both hoop and radial stress components in bi-traction loading cases.

## 6. Conclusions

The problem of failure initiation stemming from a circular hole embedded in a bidimensional domain under biaxial loading conditions was comprehensively studied herein. The analysis on the stress field and the stress intensity factor expressions revealed a complex dependence with the loading biaxiality, which influences the conditions upon failure. This variety in the prospective failure casuistry allowed for a complete assessment of the following different frameworks implemented: Finite Fracture Mechanics, in both original and averaged-stress variants; Dugdale's version of the Cohesive Zone Model; and Phase Field models of fracture, including without energy decomposition and with the No Tension decomposition. All these approaches were used to obtain hole-size dependent safety domains, and the following conclusions can be drawn:

- FFM and FFM-avg failure predictions are close, although the latter provides more conservative estimates. According to both criteria, there exist some tension-compression and compression-compression loading states for which certain range of hole sizes are associated to energy-governed failures (the aforementioned Scenario E), with no direct involvement of the stress condition.
- The agreement between FFM and CZM is generally good, although to an extent that results dependent of the loading biaxiality and the hole size. Indeed, the closeness between the failure initiation predictions of both methods is seen to improve for higher stress concentrations at failure, in line with the FFM-CZM comparisons present in the literature for different geometries. Additionally, the good tune between FFM and CZM only holds for the cases in which the failure predictions by the former are governed by both energy and stress conditions, noticeably worsening otherwise. Besides, the correlation of CZM predictions with those by FFM-avg is poorer as of the model considered, better concordance being expected should a linear softening cohesive law be used instead (see (Cornetti et al., 2019)).
- The effect of the energy decomposition in the Phase Field model of fracture is very large. In this sense, the lack of energy decomposition in the degradation of the strain energy (PF-NoSplit) yields unrealistic failure behavior, as for being symmetric in tension-compression. For this reason, the PF-NoSplit model is not further considered for comparison with Finite Fracture Mechanics and Cohesive Zone Model. On the other hand, the PF-NoTension energy decomposition leads to a behavior in much better accordance to what expected, i.e. failure is limited to develop in tensioned regions.
- The safety domains obtained through the PF-NoTension and the FFM approaches are in excellent agreement, specially when the latter is governed by the coupled criterion (Scenario C). This proves the soundness of the PF-NoTension for its use in multiaxial loading scenarios in which tension and compression stress states are present, and failure is expected to only develop in tensile regions.
- All the considered criteria are able to predict the effect of the hole size in the failure initiation load, despite the geometry being non-singular and the stress concentration factor being independent of the hole size. Indeed, this proves once again the importance of utilizing non-local failure criteria in which the critical length is associated with the energy balance upon failure.

Nonetheless, one should always keep in mind that the findings above reported are eminently theoretical results, and that only through proper experimental data they can be corroborated. In this sense, the perfor-

mance of relevant experiments that simultaneously consider the effect of the biaxiality and the hole size remains as a task to be performed in future studies. To achieve this, besides the development of a proper testing rig in which the biaxiality ratio can be varied at will, the material to be used must be carefully chosen. For instance, purely brittle materials often present very low values of  $l_{ch}$  that would also require very small holes as to capture the size effect, thus jeopardizing the representativeness of the manufactured specimens. On the other hand, quasi-brittle materials normally present larger  $l_{ch}$  values, but they are often neither homogeneous nor isotropic, which introduces a difficult-to-handle variability in the effective material properties. Likewise, the “soft” nature of the stress concentrator means that the potential near-failure non-linearities of the material would not be restricted to a very small region, as it happens for instance with failure stemming from sharp cracks.

### Author statement

A. Chao Correias: Conceptualization; Software; Writing – original draft; Visualization. A. Sapora: Conceptualization, Writing – review & editing. J. Reinoso: Conceptualization, Writing – review & editing. M. Corrado: Conceptualization, Writing – review & editing, Supervision. P. Cornetti: Conceptualization, Writing – review & editing, Supervision

### Declaration of competing interest

The authors declare that they have no known competing financial interests or personal relationships that could have appeared to influence the work reported in this paper.

### Data availability

Data will be made available on request.

### Acknowledgements



This project has received funding from the European Union’s Horizon 2020 research and innovation programme under the Marie Skłodowska Curie grant agreement No 861061.

## Annex A. Simplification of the CZM system of equations

In the present Annex, we prove that the solution of the CZM system of two equations in Eq. (23) is equivalent to imposing the first order minimality condition of the failure load with respect to the length of the process zone in the energy condition. In this sense Chao Correias et al. (2021), showed that, by merit of the Paris’ integral Paris (1957), the CZM can be implemented through a system of two equations with two unknowns entirely written in terms of different SIF expressions. In particular, the general definition of this system of equations for the problem at hand is:

$$\begin{cases} K_I(a_p, \Sigma'_1, \beta') - K_I^{\sigma_c}(a_p, \sigma_c) = 0 \\ 2E' \left( \int_0^{a_p} K_I(a, \Sigma'_1, \beta') \frac{\partial K_I^{\bar{P}}(a, \sigma_c)}{\partial a} da - \int_0^{a_p} K_I^{\sigma_c}(a, \sigma_c) \frac{\partial K_I^{\bar{P}}(a, \bar{P})}{\partial a} da \right) = \frac{G_C}{\sigma_c} \end{cases} \quad (A1)$$

where Eq. (A1) represents the stress condition of CZM and Eq. (A1) is the energy condition. Now by using Eqs. (6), (18) and (20), plus the Irwin’s relation, the following system is obtained after isolating  $\Sigma'_{1f}/\sigma_c$ :

$$\begin{cases} \frac{\Sigma'_{1f}}{\sigma_c} = \frac{F^{\sigma_c}(a_p)}{F_{\beta'}(a_p, \beta')} \\ \frac{\Sigma'_{1f}}{\sigma_c} = \frac{l_{ch} + 2 \int_0^{a_p} F^{\sigma_c}(a) F^{\bar{P}}(a) da}{2 \int_0^{a_p} F_{\beta'}(a, \beta') F^{\bar{P}}(a) da} \end{cases} \quad (A2)$$

which exactly coincides with Eq. (23).

Imposing the first order minimality condition of the failure load with respect to the process zone length in the energy condition means setting the first derivative of both sides of Eq. (A2) equal to zero:

$$\frac{\partial}{\partial a_p} \left( \frac{\Sigma'_1}{\sigma_c} \right) \Big|_{a_p=a_{p,z}} = \frac{\partial}{\partial a_p} \left( \frac{l_{ch} + 2 \int_0^{a_p} F^{\sigma_c}(a) F^{\bar{P}}(a) da}{2 \int_0^{a_p} F_{\beta'}(a, \beta') F^{\bar{P}}(a) da} \right) \Big|_{a_p=a_{p,z}} = 0 \quad (A3)$$

where  $a_{p,z}$  represents the length of the process zone that zeroes the derivatives in Eq. (A3), and so leads to the fulfillment of the first order minimization condition of the energy balance. Then, developing the derivative in Eq. (A3) results in:

$$\frac{4(F^{\sigma_c}(a_{p,z}) F^{\bar{P}}(a_{p,z})) \left( \int_0^{a_{p,z}} F_{\beta'}(a, \beta') F^{\bar{P}}(a) da \right) - 2(F_{\beta'}(a_{p,z}, \beta') F^{\bar{P}}(a_{p,z})) (l_{ch} + 2 \int_0^{a_{p,z}} F^{\sigma_c}(a) F^{\bar{P}}(a) da)}{(2 \int_0^{a_{p,z}} F_{\beta'}(a, \beta') F^{\bar{P}}(a) da)^2} = 0 \quad (A4)$$

From this point,  $F^{\bar{P}}(a_{p,z})$  can be factorized out. Additionally, since  $F^{\bar{P}}$  is strictly positive and nonzero, just as the denominator as well, the relation in Eq. (A4) can only be achieved when:



$$F^{\sigma_c}(a_{p,z}) \int_0^{a_{p,z}} F_{\beta'}(a, \beta') F^{\bar{P}}(a) da - F_{\beta'}(a_{p,z}, \beta') \left( \frac{l_{ch}}{2} + \int_0^{a_{p,z}} F^{\sigma_c}(a) F^{\bar{P}}(a) da \right) = 0 \quad (A5)$$

in turn, rearranging Eq. (A5), one obtains:

$$\frac{F^{\sigma_c}(a_{p,z})}{F_{\beta'}(a_{p,z}, \beta')} = \frac{\frac{l_{ch}}{2} + \int_0^{a_{p,z}} F^{\sigma_c}(a) F^{\bar{P}}(a) da}{\int_0^{a_{p,z}} F_{\beta'}(a, \beta') F^{\bar{P}}(a) da} \quad (A6)$$

which means that the value of  $a_p$  that zeroes the first derivative of Eq. (A2), i.e.  $a_{p,z}$  is also solution of the CZM's system of equations, i.e. it is true that  $a_{p,z} = a_{p,f}$ ,  $a_{p,f}$  being the length of the process zone at the instant of failure. Therefore, the CZM problem resolution is equivalent to solving Eq. (A5), from which  $a_{p,f}$  is obtained, and then,  $\Sigma'_{lf}/\sigma_c$  can be determined using any of the two equalities in Eq. (A2).

## References

- Abaza, A., Laurencin, J., Nakajo, A., Meille, S., Debayle, J., Leguillon, D., 2022. Prediction of crack nucleation and propagation in porous ceramics using the phase-field approach. *Theor. Appl. Fract. Mech.* 119, 103349 <https://doi.org/10.1016/j.tafmec.2022.103349>.
- Alnaes, M.S., Blechta, J., Hake, J., Johansson, A., Kehlet, B., Logg, A., Richardson, C., Ring, J., Rognes, E., Wells, G.N., 2015. The FEniCS project version 1.5. *Arch. Numer. Softw.* 3, 9–23. <https://doi.org/10.11588/ans.2015.100.20553>.
- Bleyer, J., Roux-Langlois, C., Molinari, J.-F., 2017. Dynamic crack propagation with a variational phase-field model: limiting speed, crack branching and velocity-toughening mechanisms. *Int. J. Fract.* 204, 79–100. <https://doi.org/10.1007/s10704-016-0163-1>.
- Bourdin, B., Francfort, G.A., Marigo, J.-J., 2008. The variational approach to fracture. *J. Elasticity* 91, 5–148. <https://doi.org/10.1007/s10659-007-9107-3>.
- Bourdin, B., Francfort, G.A., Marigo, J.-J., 2000. Numerical experiments in revisited brittle fracture. *J. Mech. Phys. Solid.* 48, 797–826. [https://doi.org/10.1016/S0022-5096\(99\)00028-9](https://doi.org/10.1016/S0022-5096(99)00028-9).
- Camanho, P.P., Erçin, G.H., Catalanotti, G., Mahdi, S., Linde, P., 2012. A finite fracture mechanics model for the prediction of the open-hole strength of composite laminates. *Compos. Part A Appl. Sci. Manuf.* 43, 1219–1225. <https://doi.org/10.1016/j.compositesa.2012.03.004>.
- Cavuto, B., Lenarda, P., Misseroni, D., Paggi, M., Bigoni, D., 2022. Failure through crack propagation in components with holes and notches: an experimental assessment of the phase field model. *Int. J. Solid Struct.* 257, 111798 <https://doi.org/10.1016/j.ijsolstr.2022.111798>.
- Chao Correias, A., Corrado, M., Sapora, A., Cornetti, P., 2021. Size-effect on the apparent tensile strength of brittle materials with spherical cavities. *Theor. Appl. Fract. Mech.* 116, 103120 <https://doi.org/10.1016/j.tafmec.2021.103120>.
- Cornetti, P., Muñoz-Reja, M., Sapora, A., Carpinteri, A., 2019. Finite fracture mechanics and cohesive crack model: weight functions vs. cohesive laws. *Int. J. Solid Struct.* 156–157, 126–136. <https://doi.org/10.1016/j.ijsolstr.2018.08.003>.
- Cornetti, P., Pugno, N., Carpinteri, A., Taylor, D., 2006. Finite fracture mechanics: a coupled stress and energy failure criterion. *Eng. Fract. Mech.* 73, 2021–2033. <https://doi.org/10.1016/j.engfracmech.2006.03.010>.
- Cornetti, P., Sapora, A., 2019. Penny-shaped cracks by finite fracture mechanics. *Int. J. Fract.* 219, 153–159. <https://doi.org/10.1007/s10704-019-00383-9>.
- De Lorenzis, L., Maurini, C., 2022. Nucleation under multi-axial loading in variational phase-field models of brittle fracture. *Int. J. Fract.* 237, 61–81. <https://doi.org/10.1007/s10704-021-00555-6>.
- Del Piero, G., Owen, D.R., 1993. Structured deformations of continua. *Arch. Ration. Mech. Anal.* 124, 99–155. <https://doi.org/10.1007/BF00375133>.
- Doitrand, A., Leguillon, D., 2021. Asymptotic analysis of pore crack initiation near a free edge. *Theor. Appl. Fract. Mech.* 116, 103125 <https://doi.org/10.1016/j.tafmec.2021.103125>.
- Doitrand, A., Molnár, G., Estevez, R., Gravouil, A., 2023. Strength-based regularization length in phase field fracture. *Theor. Appl. Fract. Mech.* 124, 103728 <https://doi.org/10.1016/j.tafmec.2022.103728>.
- Dugdale, D.S., 1960. Yielding of steel sheets containing slits. *J. Mech. Phys. Solid.* 8, 100–104. [https://doi.org/10.1016/0022-5096\(60\)90013-2](https://doi.org/10.1016/0022-5096(60)90013-2).
- Ferriani, F., Cornetti, P., Marsavina, L., Sapora, A., 2022. Finite fracture mechanics and cohesive crack model: size effects through a unified formulation. *Frat. Ed. Integrità Strutt.* 16, 496–509. <https://doi.org/10.3221/IGF-ESIS.61.33>.
- Francfort, G.A., Marigo, J.-J., 1998. Revisiting brittle fracture as an energy minimization problem. *J. Mech. Phys. Solid.* 46, 1319–1342. [https://doi.org/10.1016/S0022-5096\(98\)00034-9](https://doi.org/10.1016/S0022-5096(98)00034-9).
- Freddi, F., Royer-Carfigni, G., 2010. Regularized variational theories of fracture: a unified approach. *J. Mech. Phys. Solid.* 58, 1154–1174. <https://doi.org/10.1016/j.jmps.2010.02.010>.
- Kirsch, G., 1898. Die Theorie der Elastizität und die Bedürfnisse der Festigkeitslehre. *Zeitschrift des Vereines Dtsch. Ingenieure* 42, 797–807.
- Kumar, A., Bourdin, B., Francfort, G.A., Lopez-Pamies, O., 2020. Revisiting nucleation in the phase-field approach to brittle fracture. *J. Mech. Phys. Solid.* 142, 104027 <https://doi.org/10.1016/j.jmps.2020.104027>.
- Leguillon, D., 2002. Strength or toughness? A criterion for crack onset at a notch. *Eur. J. Mech. Solid.* 21, 61–72. [https://doi.org/10.1016/S0997-7538\(01\)01184-6](https://doi.org/10.1016/S0997-7538(01)01184-6).
- Leguillon, D., Piat, R., 2008. Fracture of porous materials – influence of the pore size. *Eng. Fract. Mech.* 75, 1840–1853. <https://doi.org/10.1016/j.engfracmech.2006.12.002>.
- Li, J., Zhang, X.B., 2006. A criterion study for non-singular stress concentrations in brittle or quasi-brittle materials. *Eng. Fract. Mech.* 73, 505–523. <https://doi.org/10.1016/j.engfracmech.2005.09.001>.
- Mantić, V., 2009. Interface crack onset at a circular cylindrical inclusion under a remote transverse tension. Application of a coupled stress and energy criterion. *Int. J. Solid Struct.* 46, 1287–1304. <https://doi.org/10.1016/j.ijsolstr.2008.10.036>.
- Mantić, V., Távora, L., Blázquez, A., Graciani, E., París, F., 2015. A linear elastic-brittle interface model: application for the onset and propagation of a fibre-matrix interface crack under biaxial transverse loads. *Int. J. Fract.* 195, 15–38. <https://doi.org/10.1007/s10704-015-0043-0>.
- Marigo, J.-J., Maurini, C., Pham, K., 2016. An overview of the modelling of fracture by gradient damage models. *Meccanica* 51, 3107–3128. <https://doi.org/10.1007/s11012-016-0538-4>.
- Martin, E., Leguillon, D., Carrère, N., 2012. A coupled strength and toughness criterion for the prediction of the open hole tensile strength of a composite plate. *Int. J. Solid Struct.* 49, 3915–3922. <https://doi.org/10.1016/j.ijsolstr.2012.08.020>.
- Molnár, G., Doitrand, A., Estevez, R., Gravouil, A., 2020. Toughness or strength? Regularization in phase-field fracture explained by the coupled criterion. *Theor. Appl. Fract. Mech.* 109, 102736 <https://doi.org/10.1016/j.tafmec.2020.102736>.
- Paris, P.C., 1957. The Mechanics of Fracture Propagations and Solutions to Fracture Arrest Problems - Document D2-2195. Boeing Co.
- Reinoso, J., Arteiro, A., Paggi, M., Camanho, P.P., 2017. Strength prediction of notched thin ply laminates using finite fracture mechanics and the phase field approach. *Compos. Sci. Technol.* 150, 205–216. <https://doi.org/10.1016/j.compotech.2017.07.020>.
- Rosendahl, P.L., Weißgraeber, P., Stein, N., Becker, W., 2017. Asymmetric crack onset at open-holes under tensile and in-plane bending loading. *Int. J. Solid Struct.* 113–114, 10–23. <https://doi.org/10.1016/j.ijsolstr.2016.09.011>.
- Sacco, E., 1990. Modellazione e calcolo di strutture in materiale non resistente a trazione. *Atti della Accad. Naz. dei Lincei. Cl. di Sci. Fis. Mat. e Nat. Rend. Lincei. Mat. e Appl.* 1, 235–258.
- Sapora, A., Cornetti, P., 2018. Crack onset and propagation stability from a circular hole under biaxial loading. *Int. J. Fract.* 214, 97–104. <https://doi.org/10.1007/s10704-018-0315-6>.
- Sapora, A., Torabi, A.R., Etesam, S., Cornetti, P., 2018. Finite Fracture Mechanics crack initiation from a circular hole. *Fatig. Fract. Eng. Mater. Struct.* 41, 1627–1636. <https://doi.org/10.1111/ffe.12801>.
- Strobl, M., Seelig, T., 2020. Phase field modeling of Hertzian indentation fracture. *J. Mech. Phys. Solid.* 143, 104026 <https://doi.org/10.1016/j.jmps.2020.104026>.
- Tada, H., Paris, P.C., Irwin, G.R., 2000. The Stress Analysis of Cracks Handbook, Third Edition, the Stress Analysis of Cracks Handbook, third ed. ASME Press. <https://doi.org/10.1115/1.801535>.
- Taylor, D., 2007. The Theory of Critical Distances. Elsevier, Amsterdam. <https://doi.org/10.1016/B978-0-08-044478-9.X5000-5>.
- Torabi, A.R., Etesam, S., Sapora, A., Cornetti, P., 2017. Size effects on brittle fracture of Brazilian disk samples containing a circular hole. *Eng. Fract. Mech.* 186, 496–503. <https://doi.org/10.1016/j.engfracmech.2017.11.008>.
- Weißgraeber, P., Felger, J., Geipel, D., Becker, W., 2016. Cracks at elliptical holes: stress intensity factor and Finite Fracture Mechanics solution. *Eur. J. Mech. Solid.* 55, 192–198. <https://doi.org/10.1016/j.euromechsol.2015.09.002>.
- Williams, T.N., Newman Jr., J.C., Gullett, P.M., 2011. Crack-surface displacements for cracks emanating from a circular hole under various loading conditions. *Fatig. Fract. Eng. Mater. Struct.* 34, 250–259. <https://doi.org/10.1111/j.1460-2695.2010.01512.x>.